ORIGINAL ARTICLE

Mechanical and corrosion resistance properties of AA7075-T6 sub-zero formed sheets

Rachele Bertolini[1] · Enrico Simonetto[1] · Luca Pezzato[2] · Alberto Fabrizi[3] · Andrea Ghiotti[1] · Stefania Bruschi[1]

Abstract

The poor formability of 7xxx series aluminium alloys represents the major limit to their actual use for automotive and aerospace applications. In the present study, the forming temperature effect on the mechanical, corrosion and anodization behaviours of the AA7075-T6 alloy is investigated. To this purpose, tensile tests at different temperatures, ranging from −100 to 300°C, were carried out at different rolling directions. A 6.6% increase of the ultimate tensile strength and a 28.6% increase of the uniform elongation were registered for the specimens deformed at the lowest temperature compared to highest ones. Further, the corrosion resistance of specimens deformed at ultimate tensile strength before and after anodization was increased of 85% and 95%, respectively, compared to the specimens deformed at 300°C. It was demonstrated that high deformation temperatures led to the coalescence of particles and precipitates as well as the decrease of dislocation density, which, in turn, decreased the mechanical and corrosion performances. On the contrary, the deformation temperature of −100°C was found to be the ideal one able to shorten the manufacturing process chain and improve material formability and durability during its in-service life.

Keywords Aluminium alloys · Stress/strain measurements · Hardness · Characterization · Grains and interfaces · Coatings

1 Introduction

7xxx series aluminium alloys are characterized by a very attractive combination of low density, high specific strength and corrosion resistance. Actually, they are more and more used for lightweight structural components in the automotive and aerospace industries, in which weight savings for reduced fuel consumption and exhaust emissions are mandatory [1]. However, their adoption for manufacturing sheet components is greatly limited by their scarce formability [2], and rapid degradation when exposed to the in-service environment that deteriorates their mechanical properties [3]. To this aim, the anodic oxidation process is usually applied to build a robust oxide layer on these alloys surface, in order of improving their corrosion and wear performances. The characteristics of the anodized layer strictly depend upon the microstructure of the metal matrix substrate, which, in turn, is conditioned by the manufacturing chain.

With this in mind, the present paper aims at finding an innovative forming approach able to increase the formability of AA7075-T6 sheets and, at the same time, their corrosion resistance even after anodization.

The sub-zero forming approach consists in carrying out the forming process at temperatures below the room one. Cryogenic forming was firstly introduced by [4] as an efficient method to suppress the discontinuous deformation bands—known also as Portevin-Le Chatelier (PLC) effect—responsible to the ductility reduction in 5xxx series aluminium alloys. Afterwards, it was demonstrated that the use of cryogenic forming allowed increasing the degree of deformation in correspondence of the ultimate tensile strength (UTS), which is known to be the actual limit for the component design [5].

In [6], different testing temperatures, namely from −100 to 300°C, were applied to AA6082-T6 tensile specimens. Results showed a 18% increase of the strain at necking with the respect to the value obtained at room temperature. On the contrary, a 45% reduction of the strain at necking was noticed compared to the one at room temperature tests. The same trend

✉ Stefania Bruschi
stefania.bruschi@unipd.it

1 Department of Industrial Engineering, University of Padova, Via Venezia 1, 35131 Padova, Italy

2 Department of Industrial Engineering, University of Padova, Via Marzolo 9, 35131 Padova, Italy

3 Department of Engineering and Management, University of Padova, Stradella San Nicola 3, 36100 Vicenza, Italy

was found in [7], where an increment of strain at necking from 40 to 70% was obtained with sub-zero thermal fields applied to 5xxx and 6xxx series aluminium alloys, even under different stress states. The instability onset was investigated and modelled in [8] in a wide range of temperatures and stress triaxialities. Results showed that not only the formability was improved at temperatures below zero, but also, within this temperature regime, the coarsening of intermetallic particles was prevented. This led to the preservation of the sheet initial hardness, avoiding the softening favoured by the adoption of high deformation temperatures.

Another advantage of cryogenic forming contrary to the currently used forming approaches, namely cold and hot stamping processes, lies in the reduction of the manufacturing steps to obtain the final part. Cryogenic forming consists, in fact, in just two steps, namely the cooling down of the workpiece below room temperature immediately followed by forming. On the other hand, the hot stamping process includes the following steps: (i) heating the sheet received in T4 state below 480°C, namely the solution treatment temperature, (ii) forming and finally (iii) artificially ageing [9]. A high formability is, indeed, successfully achieved thanks to the dissolution of precipitates and occurrence of recovery that take place at high temperatures together with a certain degree of plastic deformation. Nevertheless, this process chain provokes a decrease of the mechanical properties of the sheet, which imposes artificially ageing to be carried out at last. The cold stamping process is even longer: the sheets are acquired in the annealed condition state, then cold stamped and solution-heat-treated and, finally, stored at low temperature. Afterwards, sizing in the cold temperature regime is mandatory to avoid natural ageing and correct the springback [10] and possible geometrical distortions [11]. Finally, artificial ageing is carried out to achieve the necessary mechanical strength.

To further prove the reliability of the cryogenic forming method, evidences about the effect of sub-zero temperature forming on the corrosion resistance have to be given since its effect on the in-service performances of the formed parts is still unknown. In literature, solely studies relative to the effect of bulk forming processes, like forging or rolling, on the corrosion resistance, are available. Nevertheless, these technologies account for a completely different kind of stress as well as degree of deformation achieved during the process compared to the sheet metal forming scenarios and, therefore, are hardly comparable.

In [12], both room temperature and cryogenic forging operations were carried out on AA6066-T6 aluminium alloy workpieces. It was shown that the use of liquid nitrogen led to the formation of finer precipitates within the matrix, which improved the corrosion resistance after anodization, since a reduced number of particles, detrimental for the corrosion resistance, remained entrapped within the anodization film. In

[13], the corrosion resistance after anodization of a precipitation hardenable AA7075 aluminium alloy subjected to rolling at liquid nitrogen and room temperatures was studied: cryogenic-rolled specimens showed enhanced corrosion resistance, yielding the lowest corrosion current, thanks to a more homogeneous distribution of small size precipitates in the bulk material. A similar corrosion resistance improvement was achieved in [14], in which the effect of cryogenic rolling and annealing temperature on microstructure, mechanical property, and corrosion behaviour of the AA6082 aluminium alloy was investigated. The following results were achieved: (i) the cryogenic-rolled material exhibited higher corrosion resistance compared to the as-received one, thanks to the formation of higher density of dislocations inside the grains and larger density of grain boundaries that facilitated the formation of a denser oxide surface film, and (ii) cryogenic-rolled specimens followed by an annealing up to 350°C were characterized by further increased corrosion potential and decreased corrosion current, thanks to the precipitation of Mg_2Si particles and the removal of crystalline defects.

However, only a few studies have focused the attention on the potential benefits arising from sub-temperature operations in terms of mechanical and microstructural properties as well as corrosion and anodization behaviour as a function of the strain, temperature and rolling direction. Therefore, the aim of this paper is to provide a comprehensive analysis in this sense. First, mechanical tests ranging from −100 to 300°C were carried out on specimens cut at varying rolling direction. Afterwards, the specimens deformed at UTS were analysed by means of microstructural characterization, texture, nanohardness and corrosion resistance. Finally, an anodization process was carried out on those specimens deformed at UTS, and their morphological characteristics, roughness, thickness, quality and corrosion resistance were assessed. The obtained results proved a relationship between the deformation temperature and corrosion resistance properties.

2 Experimental

2.1 Material

The AA7075 aluminium alloy in the heat treated to peak ageing condition (T6) was the material under investigation. Its chemical composition (in wt%) is the following: 0.4% Si, 0.5% Fe, 1.7% Cu, 0.1% Mn, 2.0% Mg, 6.2% Zn and Al (bal) [15].

The specimens for the mechanical characterization and subsequent analyses were cut from 500 mm (width) × 500 mm (height) × 2 mm (thickness) rolled sheets, characterized by the mechanical properties given in Table 1.

Microstructural investigations using optical microscopy (OM) were performed on the as-received sheets along the

Table 1 AA7075-T6 mechanical properties in the as-received condition.

$Y_{0.2}$ (MPa)	UTS (MPa)	Nano-hardness (GPa)	Max elongation (%)
470	530	2.3	11

short transverse (ST) direction as per the ASTM-E3 (95) standard. To this aim, specimens were cut from the sheet, cold mounted, polished and etched with the Keller's solution for 20 s. The microstructure was recorded with a Leica DMRE™ OM at a magnification of ×200. Figure 1 shows the microstructure of the as-received alloy that reveals the presence of elongated pancake-shaped grains, typical of the rolling process, characterized by an average thickness, intended as orthogonal to the rolling direction, ranging between 12 and 17 μm. A very high density of precipitates is spread throughout the grains.

To identify the chemical composition of the intermetallic particles (IMPs), energy dispersive X-ray analysis (EDX) was carried out using the FEI™ QUANTA 450 Scanning Electron Microscope (SEM). Figure 2 a shows two main types of IMPs, one brighter and the other darker compared to the matrix. The former is characterized by very irregular shape and dimensions, whereas the latter assumes a polygonal aspect. The EDS spectra shown in Fig. 2b help in identifying the type of the particles, namely the bright ones correspond to Al_7Cu_2Fe, whereas the darker to Mg_2Si, in accordance to [16].

To investigate the crystallographic texture and the misorientation angle distribution, electron back-scattered diffraction (EBSD) analyses were carried out on the ST plane with an EDAX™ detector controlled by the Orientation Image
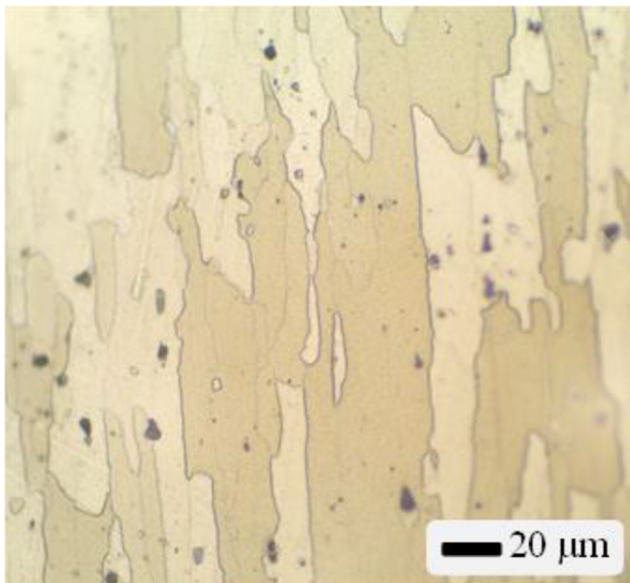
Fig. 1 OM image of the as-received AA7075-T6 microstructure along the ST plane

Microscopy (OIM™ v5.3) data acquisition software. Prior to the data collection, the specimen was firstly mechanically polished with abrasive papers, then with a diamond paste with an average particle size of 6 μm, and, finally, with a colloidal suspension of nanometric SiO_2 particles. An area of about 400 × 600 μm in the centre of the ST plane was analysed using a step size of 1 μm. Clean-up processes consisting in Grain Dilatation (GD) and Grain Confidence Index Standardization (GCIS) were conducted during EBSD data post-processing.

For the misorientation angle distributions, grain boundary angles greater than 15° were defined as high angle grain boundaries (HAGBs), whereas angles from 2 to 15° were defined as low angle grain boundaries (LAGBs) Finally, grain boundaries with angles lower than 2° were excluded from the misorientation angle distributions to avoid noise in the maps.

The inverse pole figure (IPF) map in Fig. 3a confirms the microstructure of the AA7075-T6 alloy with elongated aluminium grains, whereas the pole figures (PFs) in Fig. 3b show a crystallographic texture dominated by the typical rolling texture, as indicated in [17]. According to the grain boundaries (GBs) map (Fig. 4a) and the related misorientation angle distribution (Fig. 4b), the as-received alloy exhibits a relative low fraction of LAGBs, while most of the grain boundaries present a misorientation angle ranging from 15 to 65°.

2.2 Mechanical testing

To assess the flow behaviour of the AA7075-T6 sheets, a 50 kN MTS™-322 hydraulic dynamometer equipped with an MTS-651 environmental chamber with a temperature range from 130 (±2) °C to 315 (±2) °C was used to perform tensile tests on dog-bone specimens. The specimens were water-jet cut with the geometry shown in Fig. 5b, according to the ISO 6892 standard [18] along three directions, namely 0°, 45° and 90° with respect to the rolling one. Six testing temperatures were selected, namely −100°C, −50°C, 25°C, 100°C, 200°C and 300°C. As lowest temperature, it was chosen −100°C, being quickly and easily reachable with industrial cooling systems supplying liquid nitrogen. However, since the workpiece temperature may increase during the forming process due to the applied deformations and to the friction phenomena, the −50 °C and 25 °C were selected to characterize the material behaviour within the entire sub-zero forming process temperature window. Finally, the tests were carried out also at temperature from 100 to 300°C to investigate the behaviour of the AA707-T6 in the temperature range of the most conventional room and warm temperature forming operations.

The environmental chamber supplied liquid nitrogen through an external dewar and was used to cool the working volume till the target testing temperature. The chamber embeds also several electric heating elements to heat the working volume for testing above the room temperature. As the entire working volume is conditioned, the specimen, the tools and

Fig. 2 **a** SEM image of the as-received AA7075-T6 alloy and **b** EDS spectra of the red areas highlighted in **a**

2.3 Post mechanical testing characterization
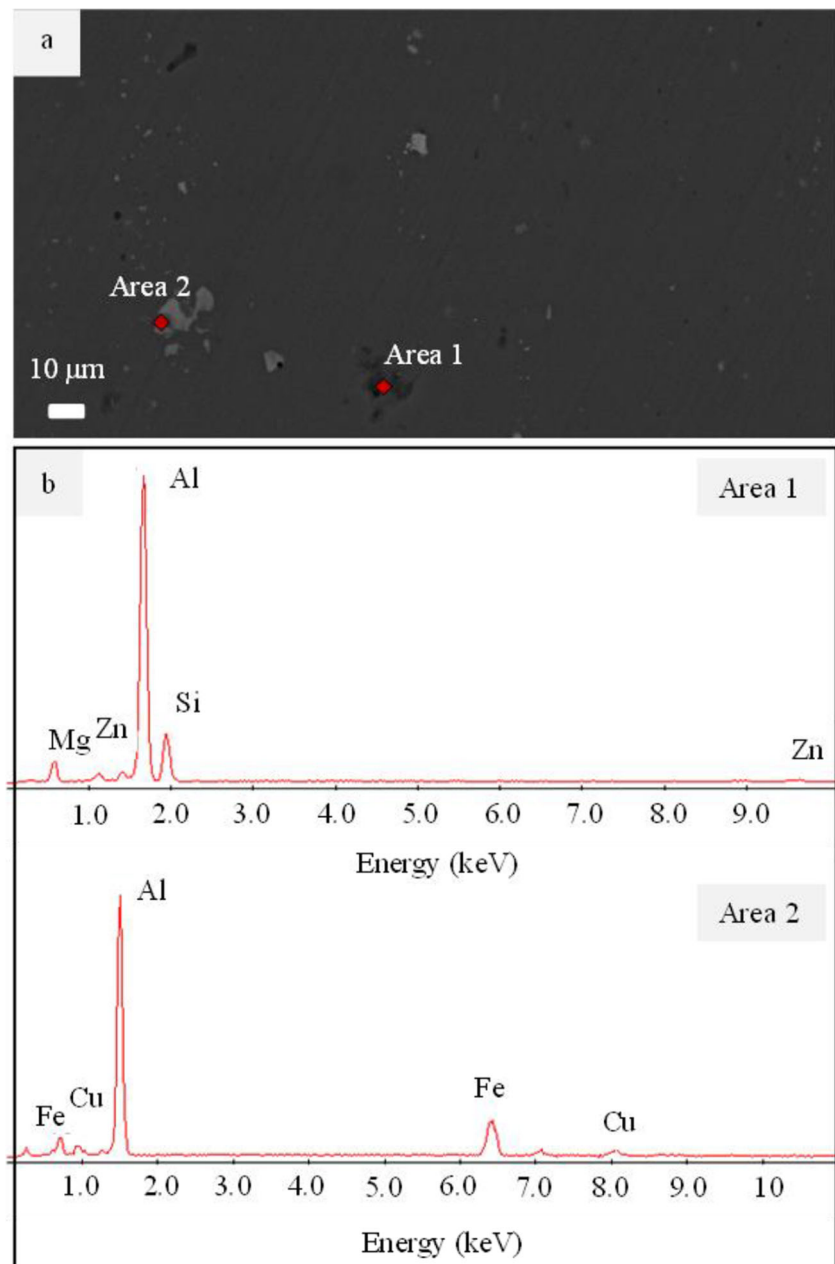
the environment are at the same temperature assuring a uniform distribution along the specimen gauge length. Figure 5 a shows the overall mechanical testing equipment, while Fig 5 b shows the inside of the environmental chamber after a test at −100°C. The specimen is gripped inside the environmental chamber between two grippers connected to the dynamometer load cell and the hydraulic piston, respectively. The use of liquid nitrogen allows reaching easily −100 °C, which was therefore chosen as the minimum testing temperature. Each tensile test was repeated 3 times for sake of repeatability with a strain rate of 0.1 s^{-1}. The latter value was chosen in compliance of the strain rate values typical of sheet stamping processes carried out on aluminium alloys [19].

Post mechanical testing characterization was performed on specimens deformed till their UTS since this is the maximum value used for designing sound sheet forming processes.

The microstructures of the UTS-deformed specimens were acquired using the procedure detailed in Section 2.1. To evaluate the amount of large IMPs particles, polished but un-etched specimens were analysed through OM at a magnification of ×200, then processing the images by the ImageJ^{TM} software.

Nano-hardness measurements was considered instead of Vickers ones with the aim of detecting strengthening mechanisms at nano-level, like density of dislocations and presence

Fig. 3 a IPF map of the as-received AA7075-T6 alloy (RD, ND and TD stand for rolling, normal and transversal direction, respectively) and **b** 001, 101 and 111 PFs
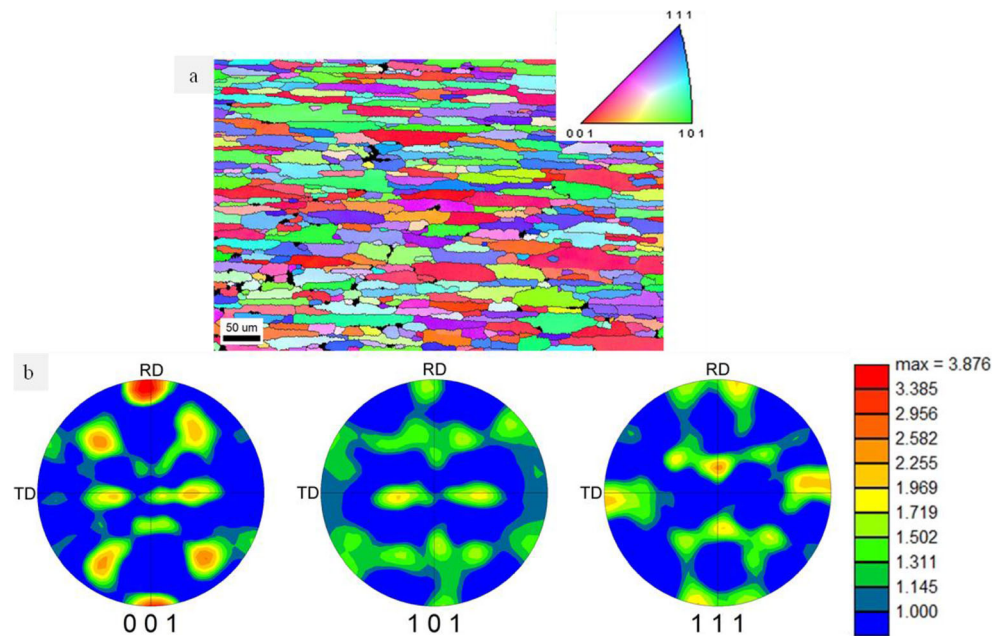
of very fine precipitates, which cannot be appreciated when adopting techniques at micro-level. The nano-hardness measurements were carried out on the iMicro™ nano-indenter with a weight of 50 mN using a Berkovich tip. Twenty-five repetitions were performed on random zones of each specimen.

The intermetallic particles inspection was performed using the Field Gun Emission Electron Microscope (FEG-SEM) FEI QUANTA™ 250 equipped with EBSD. At least three images, taken in different zones and acquired at ×50,000 and ×100,000 magnifications, were used to detect the particles dimension. The calculation procedure is shown in Fig. 6. First, the FEG-SEM images were uploaded (Fig. 6a), and a certain colour threshold value was imposed in order to clearly highlight the particles (Fig. 6b). Then, the number of particles was automatically counted by the program on the basis of their

size. In particular, three classes of particle dimension were computed on the basis of the diameter of the circumscribed circle ( ): (i) < 40 nm, called A; (ii) 40 nm < < 140 nm, called B; and (iii) > 140 nm, called C.

It is worth noting that, in order to avoid counting errors and confuse particle with pixels, the particles "A" were excluded from the calculation since they were too small to be clearly detected. An example of the difference between A and B particle classes is given in Fig. 6c.

To study the effects of the deformation temperature on the crystallographic texture and misorientation distribution, EBSD analyses were conducted on the deformed specimens by using analogous experimental procedure described in Section 2.1 for the as-received alloy.

Moreover, from the EBSD data, local strain distribution was also determined using the kernel average misorientation
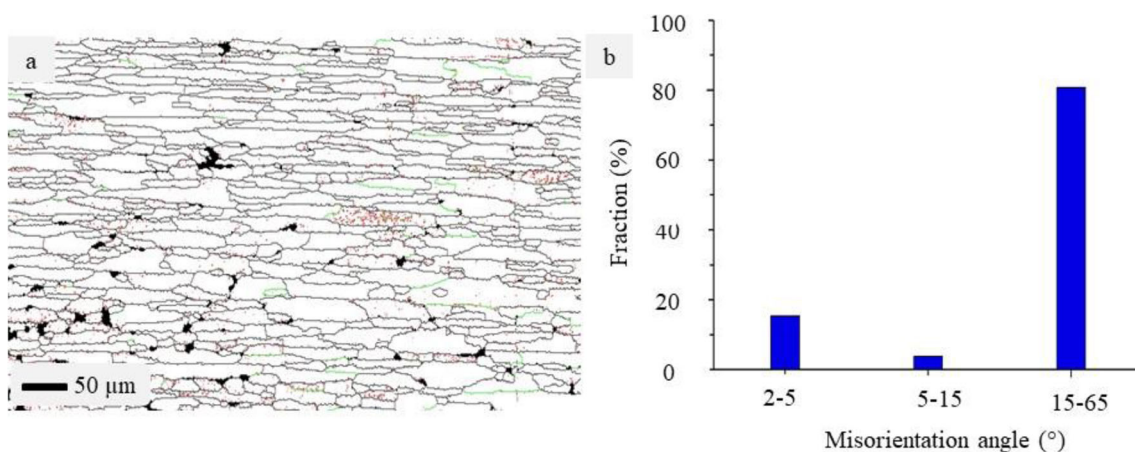
Fig. 4 a GBs map: LAGBs with misorientation angle between 2 and 5° in red lines, LAGBs between 5 and 15° in green lines and HAGBs in black lines. **b** Misorientation angle distribution

Fig. 5 a Dynamometer equipped with the environmental chamber and **b** magnified view in the case of a test carried out at −100°C
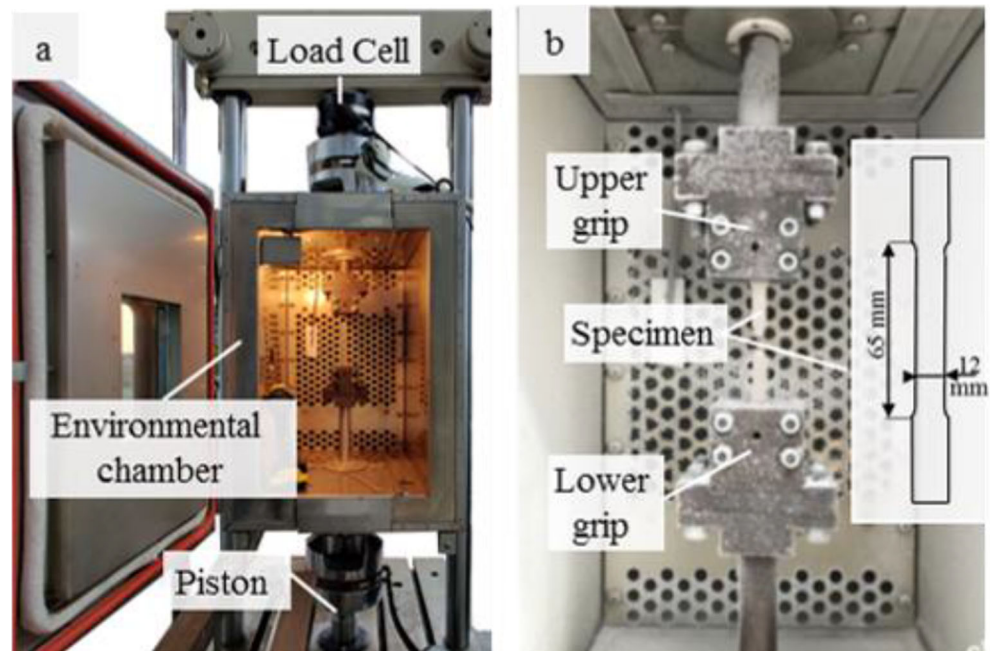
(KAM) distribution. The KAM is commonly calculated for each grain by averaging the misorientation between a given point and its nearest neighbours; it is used to estimate the local plastic strain, dislocation density, and, consequently, the strain energy stored in a material [20, 21]. In addition, the KAM is generally lower than 1° in recrystallized grains and higher in deformed ones; however, points with orientation differences larger than 5° from the centre of the kernel are excluded from the KAM distributions.

The electrochemical behaviour of the UTS-deformed specimens was evaluated using a standard three electrodes cell, where the specimens represented the working electrode, a saturated calomel electrode (SCE) the reference electrode and a platinum electrode the counter electrode.

An Amel^{TM} 2549 potentiostat was used for the electrochemical tests. The potentiodynamic polarization curves were obtained, after open circuit potential (OPC) stabilization of 1 h, applying a potential from −1.4 to 0 V at a scan rate of 0.5 mVs^{-1}. The potentiodynamic polarization curves were obtained in standard 3.5% NaCl solution. Both the corrosion potential ($Ecorr$) and the corrosion current density ($Icorr$) were extrapolated from the polarization curves, following the ASTM G5-14 standard procedure [22]. At least three tests for each condition were carried out to assure reproducibility of the results.

2.4 Anodization and sealing

Before anodizing, conventionally called anodic aluminium oxide (AAO), the UTS-deformed specimens were firstly polished until reaching a surface roughness of 0.1 μm and then ultrasonically cleaned. Subsequently, the specimens were degreased by immersion in a solution of NaOH (5 mass %) at 60°C for 30 s and then rinsed with water for 1–2 min to activate the surface. Afterwards, the pickling process was conducted, consisting in the immersion of the specimens in an
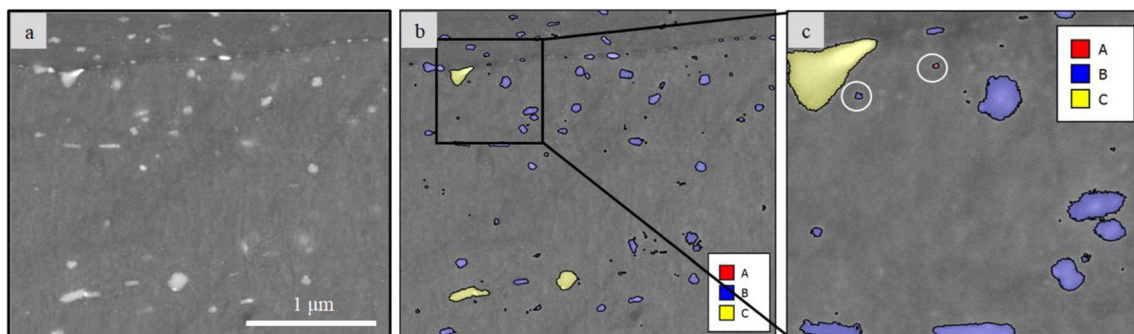
Fig. 6 Procedure for the calculation of the particle size: **a** original image acquired by FEG-SEM, **b** particles evidenced on the basis of their size, and **c** magnified image of **b** to show the difference between A and B particle classes

aqueous solution of HNO_3 (30 vol. %) for 90 s at room temperature and then rinsing with water for 1–2 min. These procedures are in accordance with those reported in [13].

Figure 7 reports the scheme of the anodization process, in which the UTS-deformed material in the form of dog-bone specimens was used as anode, whereas a piece of the same material grade stands for the cathode.

The anodization process was conducted on with a TDK-Lambda[TM] 300V/8A DC power supply at 0.05 A·cm^{-2} for 30 min. The specimens were immersed in a 15 mass % sulphuric acid solution maintained at 15°C thanks to a thermostatic bath. After anodization, a sealing treatment was carried out in water at 98°C for 20 min.

2.5 Characterization after anodization and sealing

After anodization, the specimens were firstly visually inspected, and ×3.2 low magnification images were acquired by using a Zeiss[TM] Stemi C-2000 stereomicroscope. Then, their surface roughness was measured by using a Sensofar PLu Neox™ optical profiler with a ×20 magnification Nikon™ confocal objective. The surface roughness of three different rectangular zones of 2.9 mm length and 2.2 mm width across each specimen was acquired.

To measure the thickness of the AAO layer, the specimens were cut, cold mounted and polished. The section was then inspected through SEM at ×5000 of magnification. SEM analysis was also exploited to investigate the presence of defects across the coating. To this purpose, ×10,000 images were acquired. In addition, EDS was used to identify the composition of particles entrapped within the anodization film.

Corrosion tests after anodization were also carried out by using the same procedure described in Section 2.3.

The flow chart of the overall experimental methodology is presented in Fig. 8.
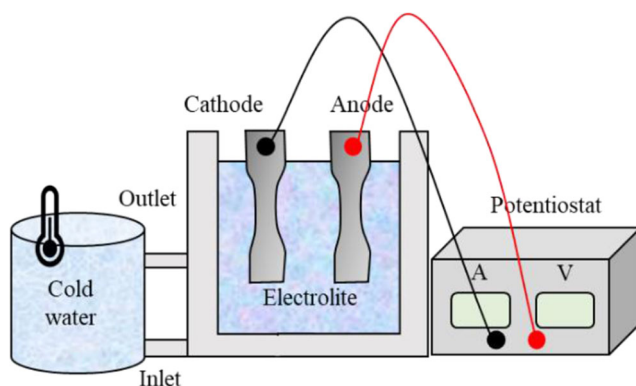

Fig. 7 Scheme of the setup used to carry out the anodization process

3 Results and discussion

3.1 Mechanical behaviour

Figure 9 shows the AA7075-T6 engineering stress-strain curves as a function of temperature and rolling direction. As the temperature rises, the material flow stress decreases, as well as the slope of the plastic strain. This shows how the strain-hardening effect is greater as the applied temperature decreases, while, as the temperature rises above 200°C, the curves appear to be almost flat or with a negative slope in plastic regime. In the latter cases, as shown in Fig. 9 e and f, not only the reached stress values are lower, but also the necking phenomena take place at lower stroke values, and therefore at lower strains. As regards the influence of the rolling direction, the specimens cut at 90° show a higher flow stress for temperatures lower than 100°C than the ones cut along 0° and 45°. Up to 100°C, the material is still deformed in cold condition, while higher forming temperatures fall within the warm range. In this range, not only a flattening of the flow-stress curves can be observed, but also a change of the relative position between the curves obtained as a function of the rolling direction.

The same trend can be seen in Fig. 10a where the UTS values are compared at varying testing temperatures and rolling direction. Furthermore, Fig. 10 b shows the UTS percentage variation taking as baseline condition the tests carried out at 25°C. It is worth noticing a mean increase of 6.6% of the UTS at −100°C and a mean decrease of 63.7% at 300°C. This means that the expected forming load for a sub-zero temperature forming process is close to the one of a conventional room temperature operation. On the other hand, forming at temperatures from 200 to 300°C implies a considerable forming loads reduction. However, at the same time, the application of a high temperature field can lower the component final mechanical characteristics. The influence of the rolling direction on the UTS percentage variation has proven to be negligible under 100°C, with relative difference between the specimens cut along three direction being under 1%. Only at higher temperature, the specimens cut along the orthogonal direction exhibit a greater drop in the UTS values, with a decrease of 28.5% compared to a mean decrease of 23.4% in the other cases at 200°C. The influence of the elevated testing temperature, 300–400 °C, on the UTS values showed similar trends to those found in [23] for AA7075-T6. It was seen that the UTS values gradually dropped at increasing temperature, as is in the present study. Actually, the intensity of both the recovery and grain boundary migration processes is reduced when the deformation occurs at sub-zero temperatures, as well as the grain coarsening and precipitates dissolution. In [23] it was asserted that the enhancement of the workpiece mechanical properties was desirable also to limit the tool friction and avoid the wrinkle onset, which represents a critical formability limit in aluminium alloy hot stamping.

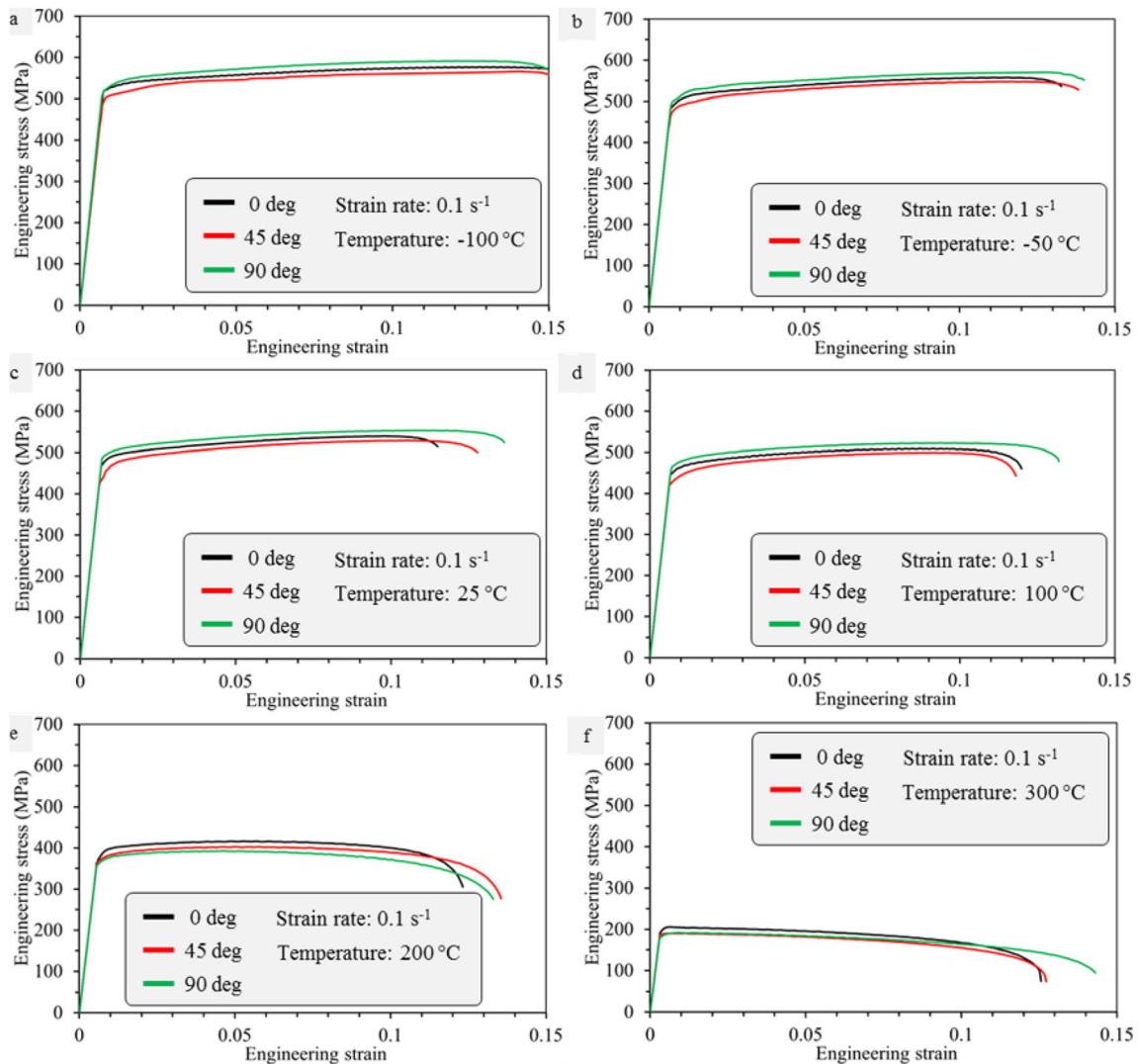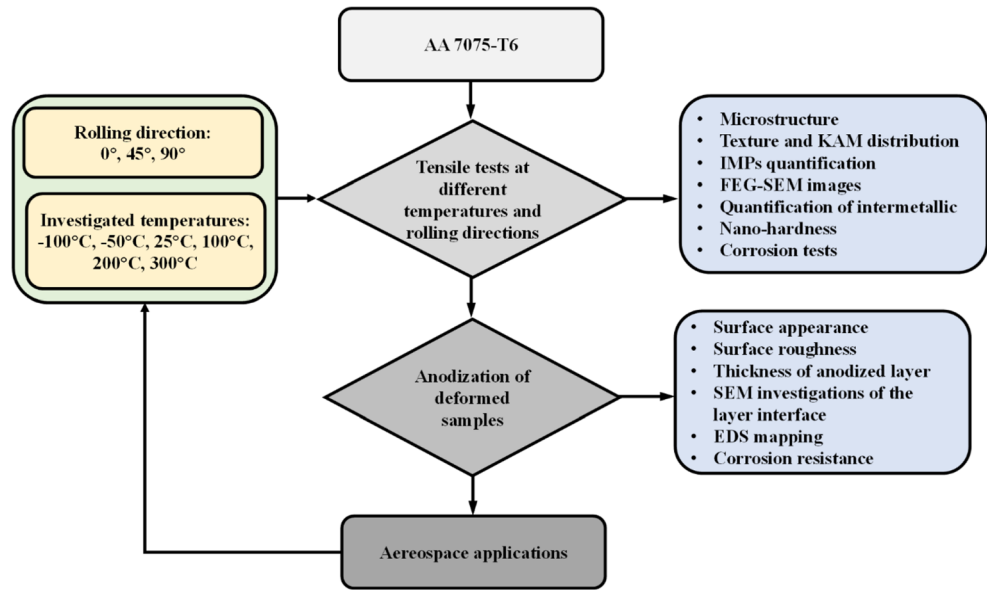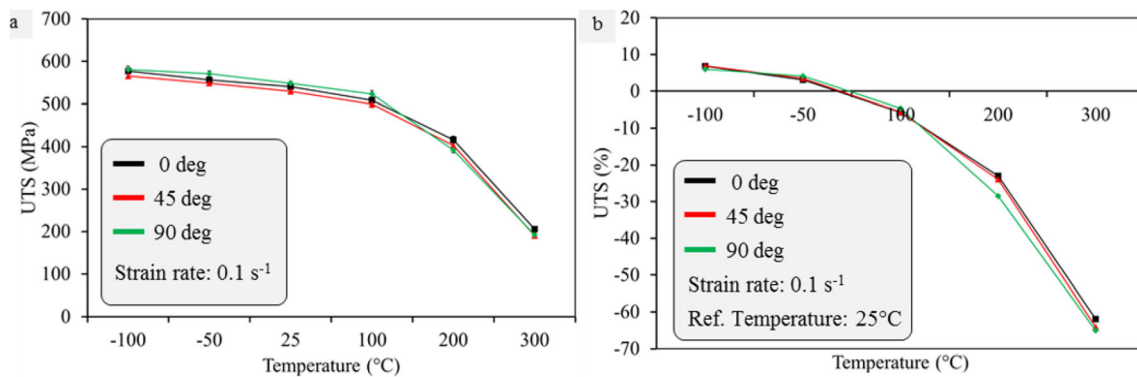**Fig. 8** Flow chart of the
experimental methodology

```
                              ┌──────────────────┐
                              │    AA 7075-T6    │
                              └──────────────────┘
                                       │
                                       ▼
┌─────────────────────────┐        ◇◇◇◇◇◇◇◇◇◇        ┌──────────────────────────────┐
│ Rolling direction:      │      ◇ Tensile tests ◇    │ • Microstructure             │
│ 0°, 45°, 90°            │─────▶◇  at different   ◇───▶│ • Texture and KAM distribution│
└─────────────────────────┘      ◇ temperatures and◇  │ • IMPs quantification        │
┌─────────────────────────┐      ◇ rolling directions◇│ • FEG-SEM images             │
│ Investigated temperatures:│      ◇◇◇◇◇◇◇◇◇◇        │ • Quantification of intermetallic│
│ -100°C, -50°C, 25°C, 100°C,│                          │ • Nano-hardness              │
│ 200°C, 300°C            │                          │ • Corrosion tests            │
└─────────────────────────┘                          └──────────────────────────────┘
```

- Microstructure
- Texture and KAM distribution
- IMPs quantification
- FEG-SEM images
- Quantification of intermetallic
- Nano-hardness
- Corrosion tests

Anodization of deformed samples

- Surface appearance
- Surface roughness
- Thickness of anodized layer
- SEM investigations of the layer interface
- EDS mapping
- Corrosion resistance

Aereospace applications

Fig. 9 AA7075-T6 engineering flow-stress at **a** −100°C, **b** −50°C, **c** 25°C, **d** 100°C, **e** 200°C, and **f** 300°C

Fig. 10. AA7075-T6: **a** UTS (mean std. dev. is contained within ± 6.2 MPa) and **b** UTS percentage variation (baseline 25 °C)

The above-mentioned increase of the strain-hardening, as the temperature lessens, is connected with the strain at necking ε^{neck} increase. Figure 11 a shows the necking strain values as a function of temperature and rolling direction. Within the tested temperature range and along all the tested directions, a temperature decrease led to an increase of ε^{neck}. This means that deformation under uniaxial condition at sub-zero temperatures postpones the starting of necking accompanied with the localized sheet thickness reduction that represents a major disadvantage of the sheet stamping processes. Taking as reference the room temperature cases, the percentage variation of ε^{neck} is shown by Fig. 11b. For all the tested directions, the maximum mean increments are reached at −100 °C and are, respectively, of 35.2%, 31.0% and 19.6%, while the mean increments drop to 13% at −50°C. However, as the testing temperature rises over the room one, the beginning of necking is reached for smaller strain values for all the tested conditions. Fig. 11b and Fig. 9 show that, as the temperature rises from −100 to 300°C, most of the plastic strain occurs in post-necking conditions, with higher true strain at fracture, but coupled with a thickness decrease. On the other hand, as the temperature lessens, most of the plastic deformation takes place before the onset of localized necking, therefore in uniform elongation conditions, which is fundamental to manufacture sound components having a constant thickness distribution.

3.2 Microstructural and thermo-mechanical characteristics after deformation

Since the effect of temperature on the alloy mechanical properties is the same regardless of the rolling direction (see Section 3.1), the characterization analyses were carried out just on the specimen at 0° direction.

Table 2 reports the average grain size of the samples deformed at UTS at varying testing temperature. The values are normalized with respect of the one of the as-received material and measured along the ST direction. It can be seen that, on average, the grain size remained unaltered after deformation. The unique exception is represented by the specimen deformed at 300°C, which shows a 20% reduction in grain size as a consequence of the recrystallization phenomenon.

The IPF maps and the pole figures of the −100°C and 200°C UTS-deformed specimens are shown in Fig. 12. Such temperatures are here reported as representative of the cold and warm regimes, respectively. It can be observed that the crystallographic textures and related intensities are substantially equivalent; moreover, they appear similar to that of the alloy in the as-received condition (see Fig. 3 for comparison). This means that the crystallographic texture was not significantly affected by the deformation temperature and conditions adopted for the mechanical testing campaign.
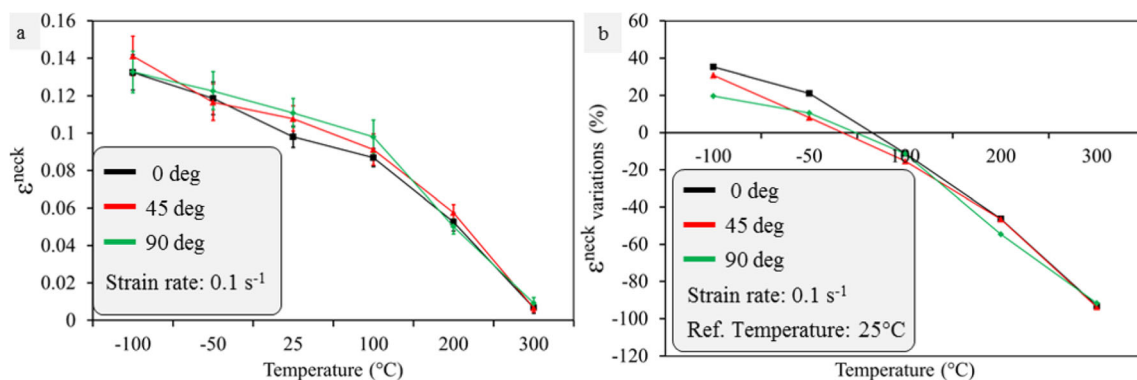
Fig. 11. AA7075-T6 **a** ε^{neck} (mean std. dev. is contained within ± 0.007) and **b** ε^{neck} percentage variation (baseline 25 °C)

Table 2 Normalized grain size of the UTS-deformed AA7075 specimens at varying testing temperature

Testing temperature (°C)	Normalized grain size
−100	1.0 ± 0.3
−50	1.0 ± 0.2
25	1.0 ± 0.2
100	1.0 ± 0.2
200	1.0 ± 0.3
300	0.8 ± 0.2

The GBs maps of the −100°C and 200°C UTS-deformed specimens are shown in Fig. 13 a and b, respectively, whereas the related misorientation distributions are compared with the one of the as-received alloy in Fig. 13c. It can be observed that the deformed specimens show a higher density of LAGBs than the as-received alloy. In

fact, as reported in [24], the fraction of LAGBs can be generally considered an indication of the localized plastic deformation in a material. Actually, the −100°C UTS-deformed specimen showed a higher fraction of LAGBs with respect to the 200°C specimen indicating that the tensile deformation at cryogenic temperature induced a higher deformed state in the material [16]. These results are in accordance with those of Fig. 11, since an increase of ε^{neck} was obtained at decreasing testing temperature.

The KAM maps and the corresponding KAM distributions of the −100°C and 200°C UTS-deformed specimens are displayed in Fig. 14 a and b, respectively, whereas the related data are summarized in Fig. 14c. It can be clearly seen that a larger fraction of green and yellow coloured regions, which correspond to the misorientation of 2° and 3°, was detected in the specimen deformed at low temperature. This can be attributed to a higher concentration of dislocations and, consequently, deformed aluminium grains.
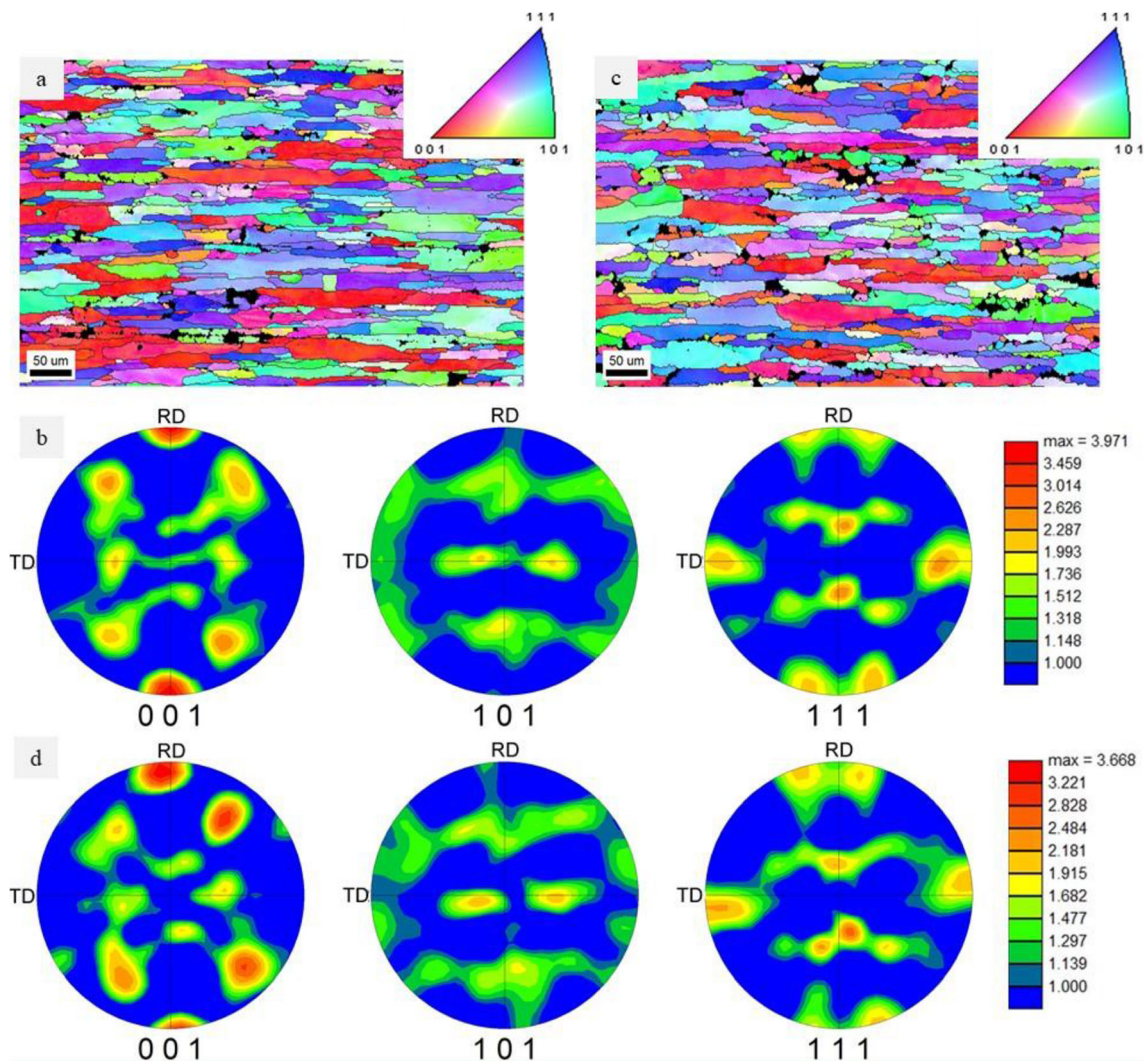
Fig. 12 **a** IPF map and **b** 001, 101 and 111 PFs of the −100°C UTS-deformed specimen. **c** IPF map and d 001, 101 and 111 PFs of the 200°C UTS-deformed specimen
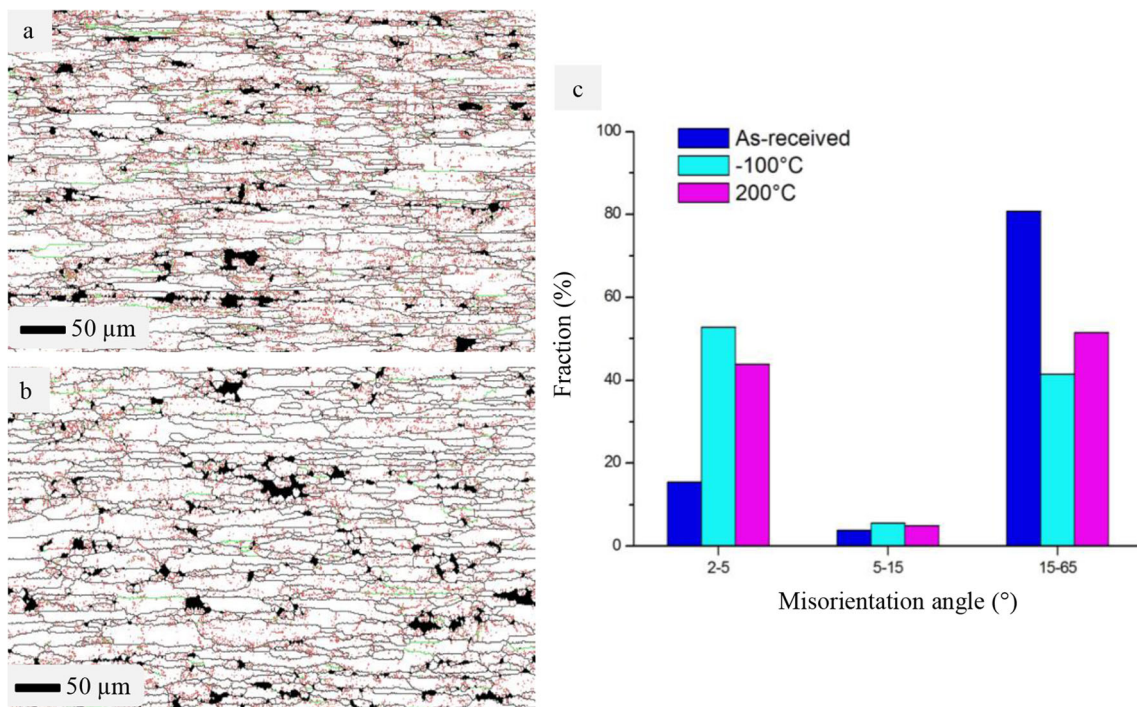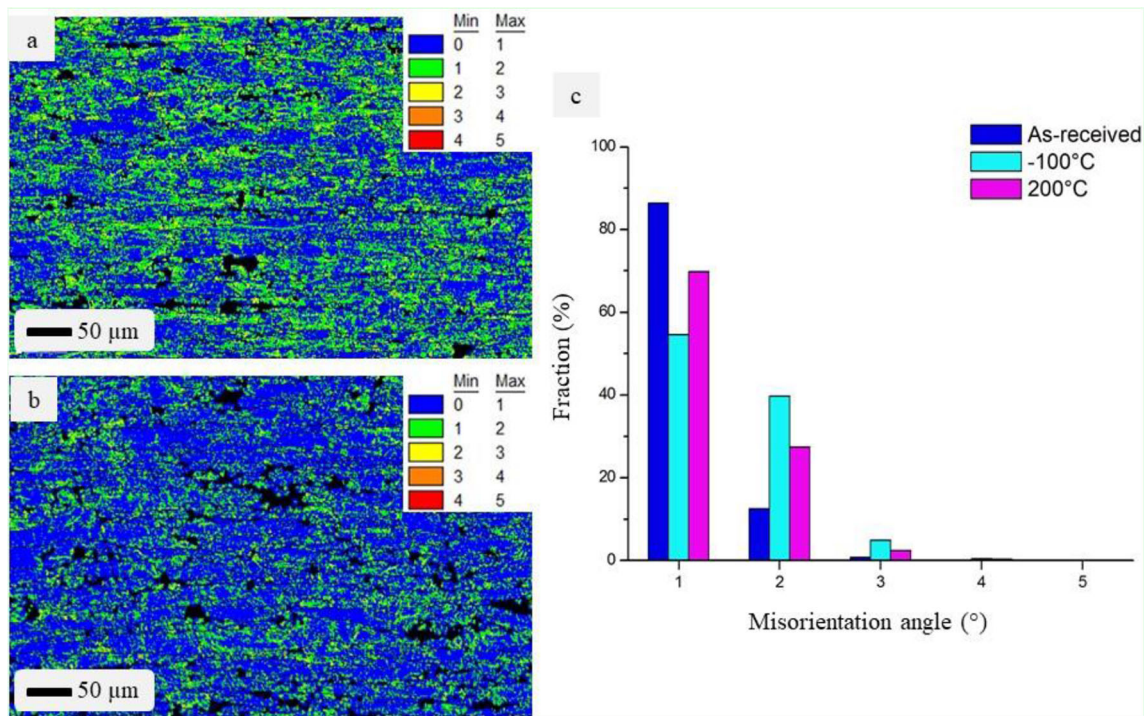
Fig. 13 GBs map along the ST plane of the **a** −100°C and **b** 200°C UTS-deformed specimens. **c** Misorientation angle distributions of the −100°C and 200°C UTS-deformed specimens (the distribution of as-received alloy is also reported)

Figure 15 graphs the amounts of IMPs per unit area for different sizes along the ST plane. A drastic increase in the number of larger particles with the respect of the as-received sheet is visible for the specimens deformed at the higher temperatures. On the contrary, the specimens deformed at −100°C, −50°C and 25°C were characterized by a lower

Fig. 14 KAM map along the ST plane of the **a** −100°C and **b** 200°C UTS-deformed specimens. **c** KAM distributions of the −100°C and 200°C UTS-deformed specimens (the distribution of as-received alloy is also reported)
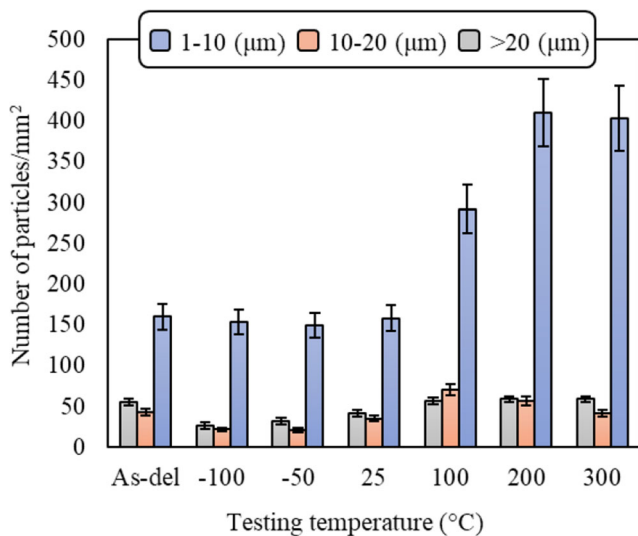
Fig. 15 IMPs of the UTS-deformed AA7075 specimens at varying testing temperature

number of large particles, even lower than the one of the as-received material. The same trend applies also for the other particle size.

The phenomenon of particles coalescence depended on the temperature at which the deformation occurred. High temperatures gave the particles enough energy to increase their size. On the contrary, low temperature in combination with applied strain favoured the particle fragmentation.

A close-up view of the microstructure was feasible by using the FEG-SEM and is reported in Fig. 16, whereas Fig. 17 shows the particle analysis results. By comparing Fig. 16 a,

b and c, it can be seen that a significantly higher amount of precipitates was present in the specimen deformed at −100°C compared to the one deformed at 200°C. Actually, on the latter, several precipitates free zones (PFZ), distinguished by lack of precipitates, are visible as well as relatively large IMPs (evidenced by white circles) according to what previously reported.

Figure 16 d, e and f help in determining the type of particles present in the alloy: the plate-like/needle-shaped particles and spherical-shaped particles correspond to the Guiner-Preston (GP) zones and η' phase, respectively. The former are small clusters of zinc-rich atomic semi-coherent layers, whereas the η' phases are $MgZn_2$ (η' and η) precipitates characterized by a size ranging from 1 to 100 nm. In general, finer precipitates are present inside the grains, whereas their size is higher at the grain boundaries, due to preferential diffusion of the solute at the grain boundaries compared to the material matrix [25]. Even GP zones and η have similar morphologies: the former are thinner and often also longer than the latter. Finally, IMPs are usually larger than 1 μm.

Precipitates are of great importance for mechanical properties: these coherent nanosized precipitates act as obstacles for the dislocation movement due to tensile straining. The density of η' precipitates in the −100°C deformed specimen was higher, and, consequently, the inter-distance between particles was lower compared to the 200°C deformed specimen and to the base alloy.

Results of nano-hardness measurements carried out on the ST plane are reported in Fig. 18. Harder surfaces compared to the as-received material were obtained solely in the case of
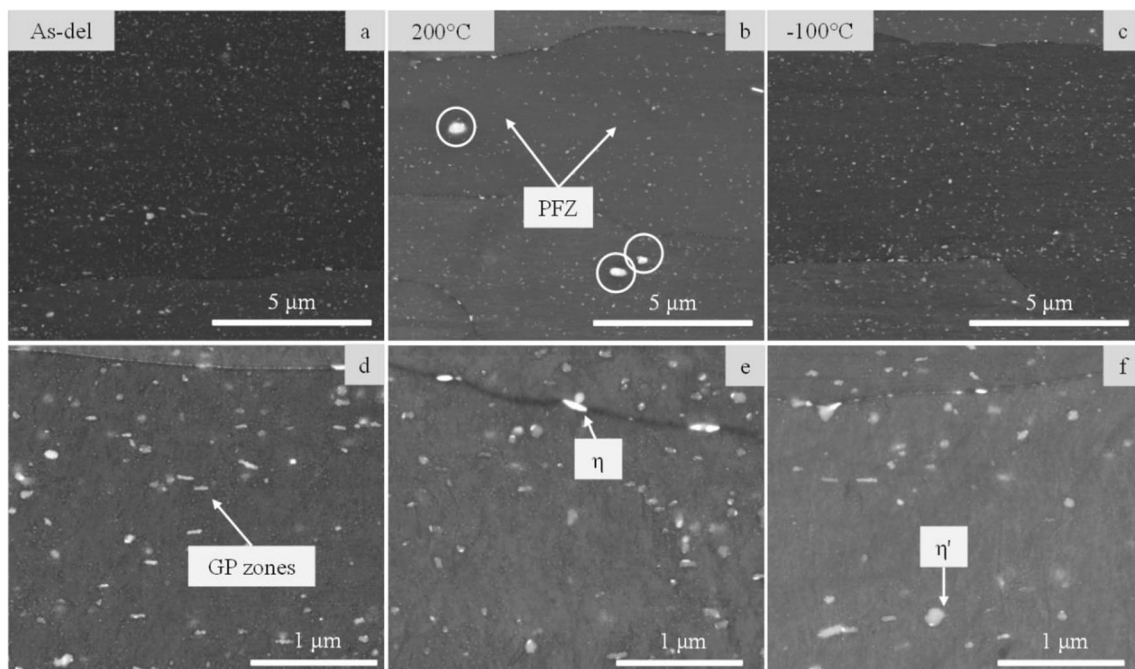
Fig. 16 FEG-SEM images of the as-delivered (**a** and **d**) and UTS-deformed AA7075 specimens at 200°C (**b** and **e**) and −100°C (**c** and **f**)
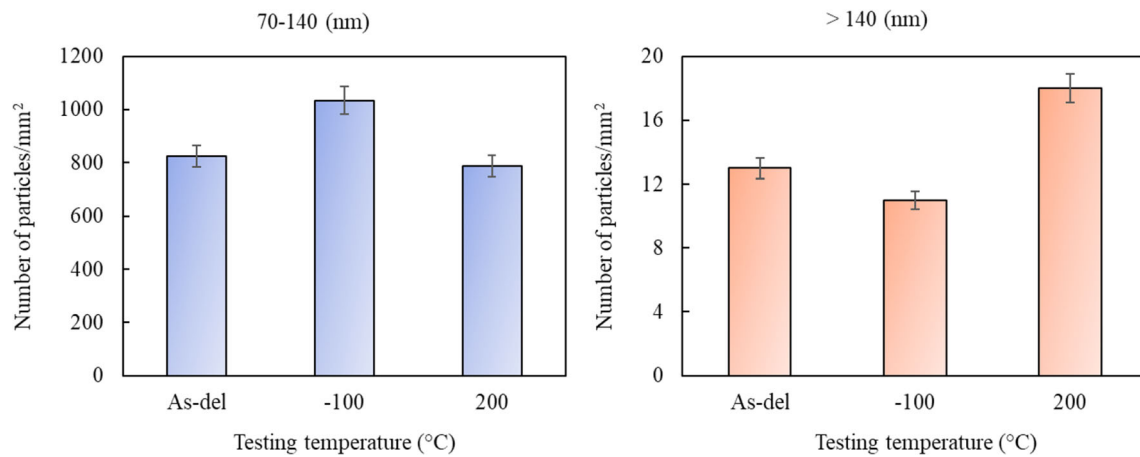
Fig. 17 Precipitates of the UTS-deformed AA7075 specimens at varying testing temperature

deformation at −50°C and −100°C. Specifically, considering the specimen deformed at 25°C, a 11% and 16% nano-hardness increase was registered for the specimens tested at −100°C and −50°C, respectively. On the contrary, a 35% decrease was found for the specimen tested at 300°C.

Deforming at low temperatures resulted in higher storage energy, which might provide a higher driving force for grain boundary migration as well as reduction of recovery. Moreover, the decrease of deformation temperature impaired the coalescences of the IMPs [23].

3.3 Strengthening mechanisms at varying testing temperature

Results reported in Section 3.1 show that the mechanical properties of the AA7075-T6 alloy are strictly dependent upon the testing temperature. A 6.6% and 28.6% increase of UTS and ε^{neck} was registered for the specimens tested at the lowest temperature with the respect to the ones tested at the highest temperature. Regardless of the rolling direction, the uniform
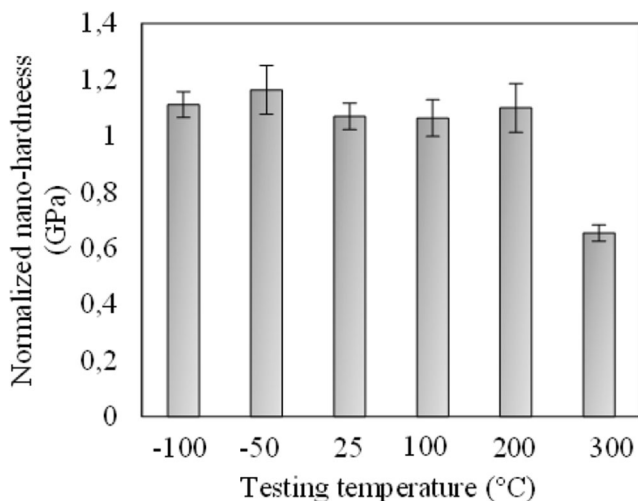
Fig. 18 Normalized nano-hardness of the UTS-deformed AA7075 specimens at varying testing temperature

elongation values showed an indirect relationship with the mechanical testing temperature, delaying the necking starting.

It can be clearly seen from the experimental data of Fig. 9 and Fig. 18 that specimens deformed at sub-zero temperatures are characterized by improved mechanical strength and nano-hardness compared to the specimens deformed at the other temperatures.

According to [26], solid solution strengthening, grain refinement, dislocation strengthening and precipitation hardening mainly contribute to the mechanical strength of the AA7075-T6 alloy.

Solid solution strengthening is related to the amount of the solute in the solid solution, which determines the formation of substitutional or interstitial point defects, thus affecting the strain field in the matrix [27]. Nevertheless, every sheet was in T6 condition; therefore, the solid solution strengthening cannot be the reason of the different strength values obtained at varying temperatures.

The grain refinement strengthening refers to the Hall-Petch relationship, which foresees that the strength is directly related to the average grain size through the Hall-Petch coefficient [28]. Table 3 reveals that, excluding the material deformed at the highest temperature, the average grain size was not affected by the testing temperature. Therefore, the size of the grains cannot be considered the reason for the strength improvement shown by the sub-zero deformed specimens.

Table 3 Electrochemical data obtained from potentiodynamic polarization curves at varying testing temperature

Testing temperature (°C)	I_{corr} ($\mu A/cm^2$)	E_{corr} (V)
−100	1 ± 0.5	−1.03 ± 0.1
−50	3 ± 0.8	−1.04 ± 0.1
25	2 ± 1	−1 ± 0.05
100	3 ± 0.7	−1.04 ± 0.1
200	4 ± 1	−1.06 ± 0.05
300	6.5 ± 1	−1.07 ± 0.1

Dislocation strengthening is connected with the amount of dislocations present within the material. As witnessed by the sharp slope of the curve of the specimen deformed at the lowest temperatures (see Fig. 9), dislocation density is remarkably increased in those specimens compared to the one of the specimens deformed at higher temperatures. This can be attributed to the suppression of dynamic recovery and restriction of dislocation movements, like cross slip and glide. In [17], an inverse relationship between dislocation density and temperature increase was proposed on the basis of high resolution transmission electron microscopy images. In addition, KAM distribution of Fig. 14 further proves the increase of dislocations and energy stored in the material at lower temperatures, as witnessed by the rise of 2° and 3° fraction angles.

Precipitation hardening refers to the presence of precipitates, which can hamper dislocation motion by interfering with their movement. In general, a higher number of small precipitates boost the strength of the material [29]. On the basis of Fig. 17, it can be said that precipitation strength is the highest for the specimen deformed at −100°C compared to the one of the specimen deformed at 200°C, thanks to the finer and more homogeneously dispersed precipitates that strongly oppose the dislocations movements.

On the basis of the present discussion, solely dislocations and precipitation strengthening are the responsible of the strength improvement of the AA7075-T6 alloy at sub-zero temperatures.

Even if the IMPs do not play a direct role in affecting the strength of the AA7075 alloy, they represent a crack initiation trigger. In fact, they favour the formation of PFZ, which are characterized by poor mechanical properties, as shown in Fig. 16b [6]. Figure 15 shows that the specimens deformed in the temperature range between −100 and 100°C present a reduced number of large IMP even compared to the as-received material. Contrarily, a drastic increase is seen for the specimens deformed at the highest temperatures.

Similar to σ_0, also ε^{neck} is not reduced at increasing testing temperature. This behaviour is characteristic of face centred cubic (FCC) metals with high stacking fault energy (SFE). For aluminium alloys, SFE lies between 160 and 200 mJ*m^{-2} [30], meaning that both dislocation movement and dynamic recovery are facilitated [31]. By carrying out deformation at very low temperatures, the dynamic recovery phenomena are suppressed, inhibiting dislocation movements, effectively delaying the formation of geometric instabilities at high strain.

3.4 Corrosion resistance after deformation

As stated in the Introduction, pitting corrosion is one of the main problems that impair the structural integrity of mainly aerospace components, after having been in service for a long period in contact with the corrosive atmospheric environment. Pitting usually takes place after the cracking of the passive layer as a consequence of the interplay of the surface with the ionic species present on the environment that can penetrate through the film and locates in correspondence of atom vacancies [32]. Thus, the underlying metal starts corroding. Pitting usually evolves in four stages: (i) rupture of the film, (ii) fast growth of metastable pits, (iii) stable pit grow over a longer period and (iv) repassivation [33].

In the present study, sodium chloride is used as electrolyte since chlorides are abundant in the environment and represent the main cause of pitting corrosion [34].

Figure 19 reports the potentiodynamic polarization curves for the specimens tested at different temperatures, whereas Table 3 summarizes the corrosion data derived from the figure. Both the E_{corr} and I_{corr} can be used as indicators of a material resistance to corrosion. In particular, the higher the value of the former and the lower the value of the latter, the better the metal resistance to corrosion. From Table 3, no significant differences of E_{corr} between the investigated specimens were observed. However, a significant decrease in I_{corr}, namely 85%, was observed for the specimen deformed at −100°C compared to the one of the specimen deformed at 300°C. Overall, the specimens deformed at temperatures ranging from −50 to 100°C show similar behaviour, whereas a slight worsening is found for the specimen deformed at 200°C. These observations imply that deformation at 200°C and 300°C induces a corrosion resistance reduction.

3.5 Factors affecting corrosion resistance as a function of the mechanical testing temperature

Corrosion resistance of aluminium alloys is still an open subject in literature. From a viewpoint of metallurgy, corrosion is usually associated with structural inhomogeneities due to precipitates, interfaces and other defects.

The role of constituent particles in the pitting corrosion of AA7075-T6 in an aerated 0.5M NaCl solution was studied in [34]. Two types of particles were identified, namely anodic (type A) with respect to the matrix that tend to dissolve and cathodic (type B) with respect to the matrix that tend to promote dissolution of the adjacent matrix. Analyses by SEM and EDS were shown that type A particles were those containing Al, Cu, Mg and Zn and type B particles were those with Al, Fe, Cu, Mn and Zn.

Several studies were devoted to evaluate the effect of different particles on aluminium alloy corrosion resistance. In [35], the corrosion damage occurrence was found in correspondence of Al$_7$Cu$_2$Fe IMPs. In particular, "peripheral" type of corrosion was encountered, which refers to the pitting at particle-matrix interface. In fact, cathodic particles are known to support appreciable oxygen reduction reaction (ORR) that causes the dissolution of the matrix to maintain the net current balance upon the alloy surface. Peripheral pitting is also referred to as "trenching" in many studies.

Fig. 19 Potentiodynamic polarization curves obtained in 3.5% NaCl solution at room temperature at varying testing temperature
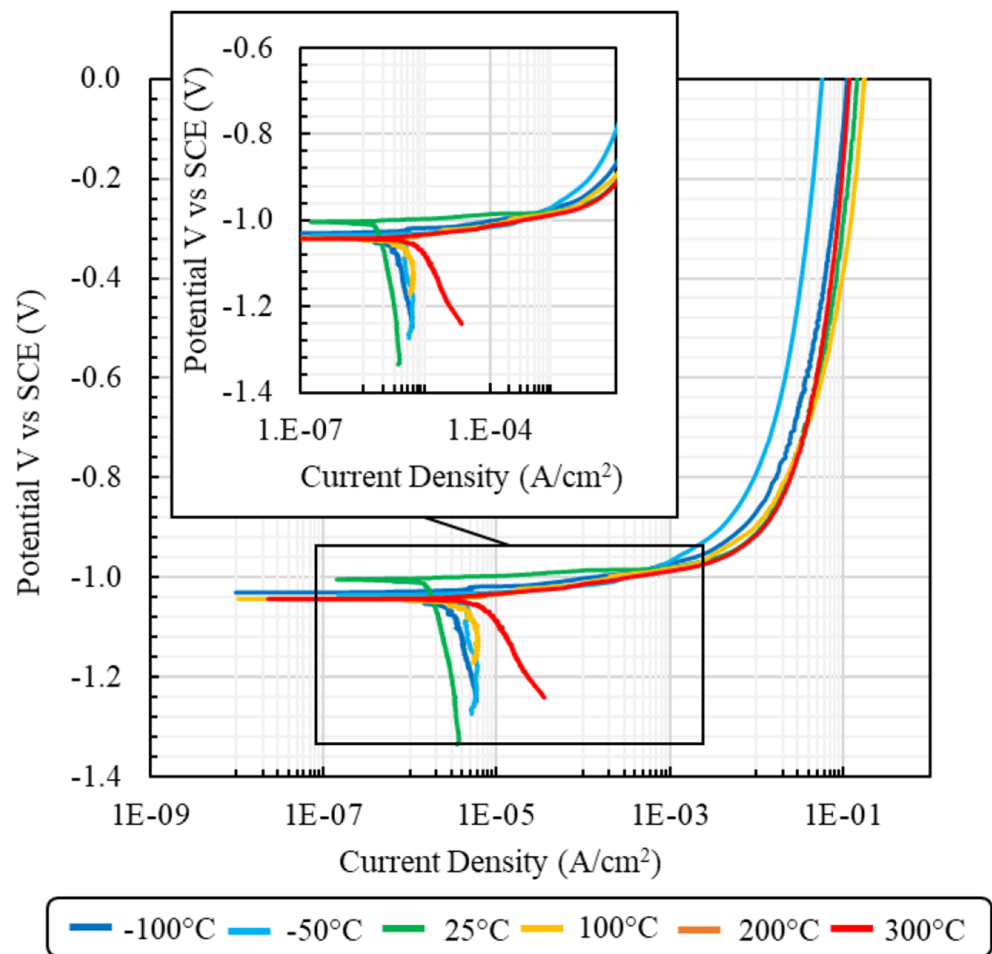
In [36], the intergranular corrosion of 7xxx series aluminium alloys was attributed to the anodic dissolution of η precipitates at grain boundaries that represent a chimney of intergranular corrosion. However, not only the type of particles but also the characteristics of particles population were highlighted to be of primary importance in the localized corrosion of Al-Zn-Mg-Cu alloys. In fact, too large IMPs were recognized to have a primary role in determining the galvanic interactions with the matrix [37, 38]. This raised concerns regarding material failure associated with IMPs during service by localized corrosion and stress corrosion cracking or environment-assistant cracking.

In [39], the effect of equal-channel angular pressing (ECAP) on the pitting corrosion resistance of AAO Al-Cu alloy was investigated. The time required before initiating pitting corrosion of the AAO Al-Cu alloy was longer with ECAP than without, indicating that the ECAP process improved the pitting corrosion resistance of the AAO Al-Cu alloy. Second phase precipitates were present in the alloy matrix, and the size of these precipitates was greatly decreased in case of ECAP.

In [40], the behaviour of the Al_7Cu_2Fe precipitate in AA7475-T7351 and AA7081-T73511 aluminium alloys was

evaluated in terms of microstructural characterization and polarization tests. A lower corrosion current density was found for the latter alloy, due to the presence of Al_7Cu_2Fe more elongated and finer particles compared to the ones of the other alloy. The possible reason was ascribed to the manufacturing process: the AA7081-T73511 was extruded whereas the AA7475-T7351 hot rolled. The extrusion process caused more severe stretching and, consequently, made increase the particle fragmentation.

Besides precipitates and IMPs, also the density of dislocations is known to be a preferential way to accelerate corrosion [41]. In [42], a stress corrosion cracking (SCC) resistance improvement was found for the AA7075 alloy thanks to the retrogression and reageing (RR) treatment compared to the T651 condition. The RRA consists in a double ageing treatment, with a retrogression step in between. The improvement in SCC for RRA-treated specimens was attributed to the reduction in dislocation density adjacent to grain boundaries and in the bulk of the grains thanks to the applied thermal treatment. In this study, it was found that pitting per se was not sufficient to initiate cracking under a stress condition. The additional stress contribute was given by dislocations that acted as site for hydrogen concentration.

In the present study, the same type of particles was present in the alloy as witnessed by the presence of similar particles morphology on FEG-SEM images of Fig. 16. Nevertheless, the size of particles was greatly affected by the temperature at which the mechanical testing took place. From Figs. 15 and 17, it can be seen that the particle size increased monotonically with the testing temperature. This means that the corrosion attacks may be more severe in the case of the specimen deformed at 300°C, as witnessed by its higher corrosion current density. On the contrary, the amount of dislocations is inversely proportional to the testing temperature, as demonstrated by the increase of strain hardening coefficient. This would have led to a corrosion resistance decrease. However, on the basis of the findings of the present study, the effect played by the particle size exceeded the one played by dislocation accumulation.

3.6 Anodization film characterization

Aluminium and its alloys generally possess good corrosion resistance under ambient conditions due to the spontaneous formation of a protective surface oxide layer [43]. However, this native oxide layer is very thin and provides limited corrosion resistance to the metal. In this framework, the electrochemical anodization process is widely used as surface treatment of aluminium alloys for industrial applications in order to increase the thickness of the oxide layer and, thus, achieve a higher corrosion resistance [44].

Figure 20 shows the AAO specimens at varying testing temperature. The colour is clearly dependent upon the testing temperature, having an intense gold-like appearance at −100°C that converts into a grey colour for the specimen tested at 300°C. Similarly, the colour of the specimen deformed at 200°C is a different nuance compared to the one of the specimens deformed 100°C, 25°C and −50°C, which instead are very similar.

It is worth noting that only the specimens deformed at 200°C and 300°C appear studded by black spots visible at naked eye. As different colouring is usually attributed to surface roughness change [45], the surface roughness Sa of the investigated specimens was measured and is reported in Fig. 21.

Except for the specimens deformed at −100°C, Sa settles at approximately 0.5 μm. The roughest surfaces were, instead, obtained in the case of specimens deformed at the coldest and hottest temperature with an increment of 469% and 57% compared to the material tested at 25°C, respectively. Rougher surfaces produce different anodization colouring due to different light absorption of the surface. However, the surface roughness trend does not explain the black spots present at the highest testing temperature as well as the grey colour obtained in the case of the 300°C deformed specimen. For this reason, the specimen surfaces were also analysed with the stereomicroscope, and the resulting images are reported in Fig. 22. The images show that the surfaces are sprinkled of particles, highlighted by arrows, aligned towards the rolling direction. Nevertheless, the size and distribution of particles depend on the testing temperature. It can be seen that the highest number of particles characterized the specimen deformed at the lowest temperature, whereas at the highest temperature, they became less spread, but larger. Such particle distribution reflects the one that were present in the substrate (see Fig. 15). The presence of black spots can be associated to the formation of relatively large cavities, which occurs in correspondence of coarse IMPs, characterized by the preferential dissolution of these particles during anodizing in the sulphuric bath.

Figure 23 summarizes the coating thicknesses calculated on the basis of the SEM images of the cross-sections reported in Fig. 24. In general, the coating appears very homogeneous on the entire surface of each specimen, as witnessed by the reduced standard deviation. Nevertheless, the coating thickness does not show a dependence from the mechanical testing temperature. Thickest coatings were achieved in the case of the −100°C and 100°C deformed specimens, whereas the thinnest in the case of −50°C. Nevertheless, this may be attributed to an intrinsic variability of the coating thickness, since the overall variation is less than 9%.

On the contrary, a closer observation of the images reported in Fig. 24 reveals the presence of defects whose size and

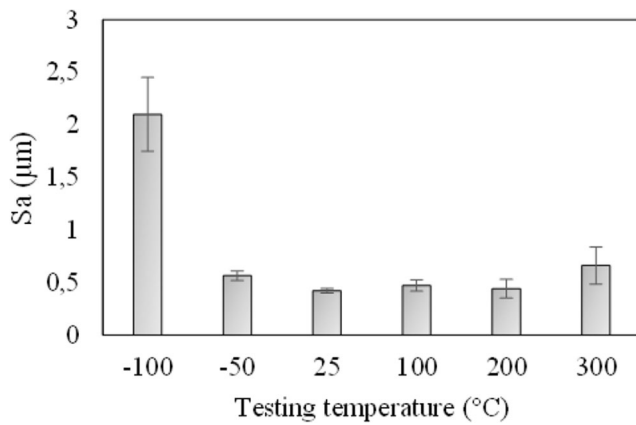Fig. 20 Appearance of the AAO film at varying testing temperature
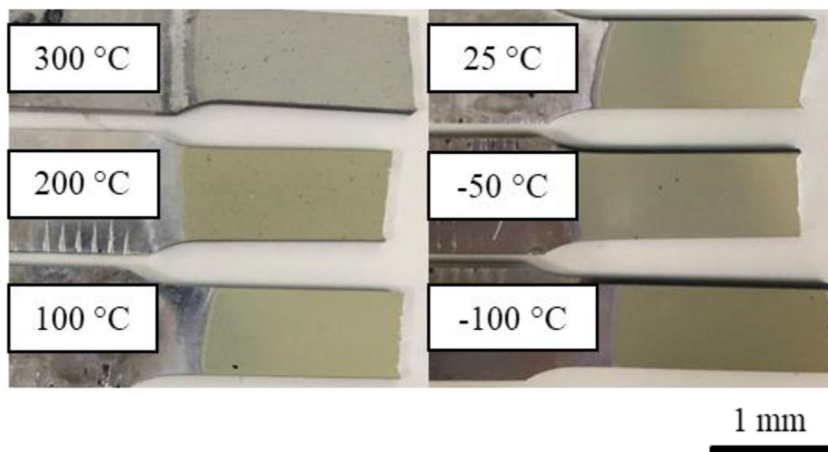
Fig. 21 Surface roughness at varying testing temperature

Fig. 23 Anodization coating thickness at varying testing temperature

dimension depend upon the testing temperature. At increasing testing temperature, more defects characterized the AAO coating. In addition, in correspondence of the IMPs, irregularities or flaws appeared in the coating (see the dotted red lines that represent the interface between the substrate and the AAO film). The best coating quality pertains to the specimen deformed at −100°C, since an almost defects-free layer was formed.

In [14], the sensitivity of the anodization coating upon the matrix microstructure was studied, comparing specimens deformed at room temperature and with the abduction of liquid nitrogen with the material in the as-received condition. It was found that the anodization layer characterizing the starting material was rich of defects due to the presence of coarser IMPs. On the contrary, shearing produced by rolling led to particle fragmentation and, therefore, improved the AAO film quality.

Detailed investigation of the coating quality is reported in Fig. 25, which shows ×10,000 magnified SEM images of the cross-section of the specimens at varying testing temperature. These images witness that the presence of IMPs played an
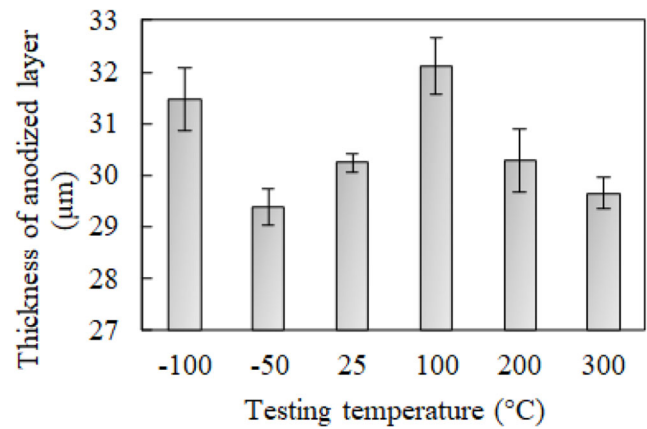
important role on the AAO film formation. In fact, to a particle entrapped within the film corresponds the formation of a concavity of the film interface when the particle is near the substrate, or the formation of cracks that can extend up to the surface when the particles are located far from the substrate.

The particles trapped within the AAO film were characterized by EDS analysis whose results are reported in Table 4, whereas the EDS map is shown in Fig. 26. White particles contain mainly Fe-Cu-Zn and are surrounded by voids, as witnessed by the increase of C detection relative to concentration of impurities within flaws, whereas Mg-Si particles are present in case of a concave AAO layer/interface.

These kinds of defects can be explained on the basis of the IMPs characteristics, as IMPs are oxidized at different rates compared to the surrounding aluminium matrix. The electrochemical nobility and anodization propensity of aluminium alloys are highly dependent on their microstructure and, in particular, on the particle nobility as discussed in Section 3.5. During AAO, Al_7Cu_2Fe-type constituent particles remain stable, whereas peripheral dissolution occurs in the closest vicinity of these particles leading to the formation
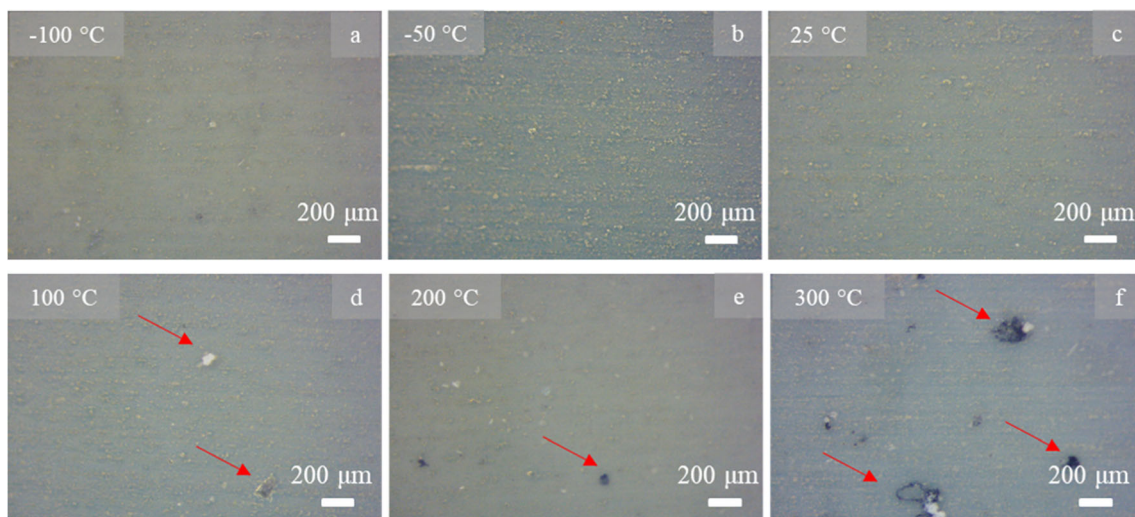

Fig. 22 Surface appearance of the AAO film at varying testing temperature: **a)** -100°C, **b)** -50°C, **c)** -25°C, **d)** 100°C, **e)** 200°C, **f)** 300°C
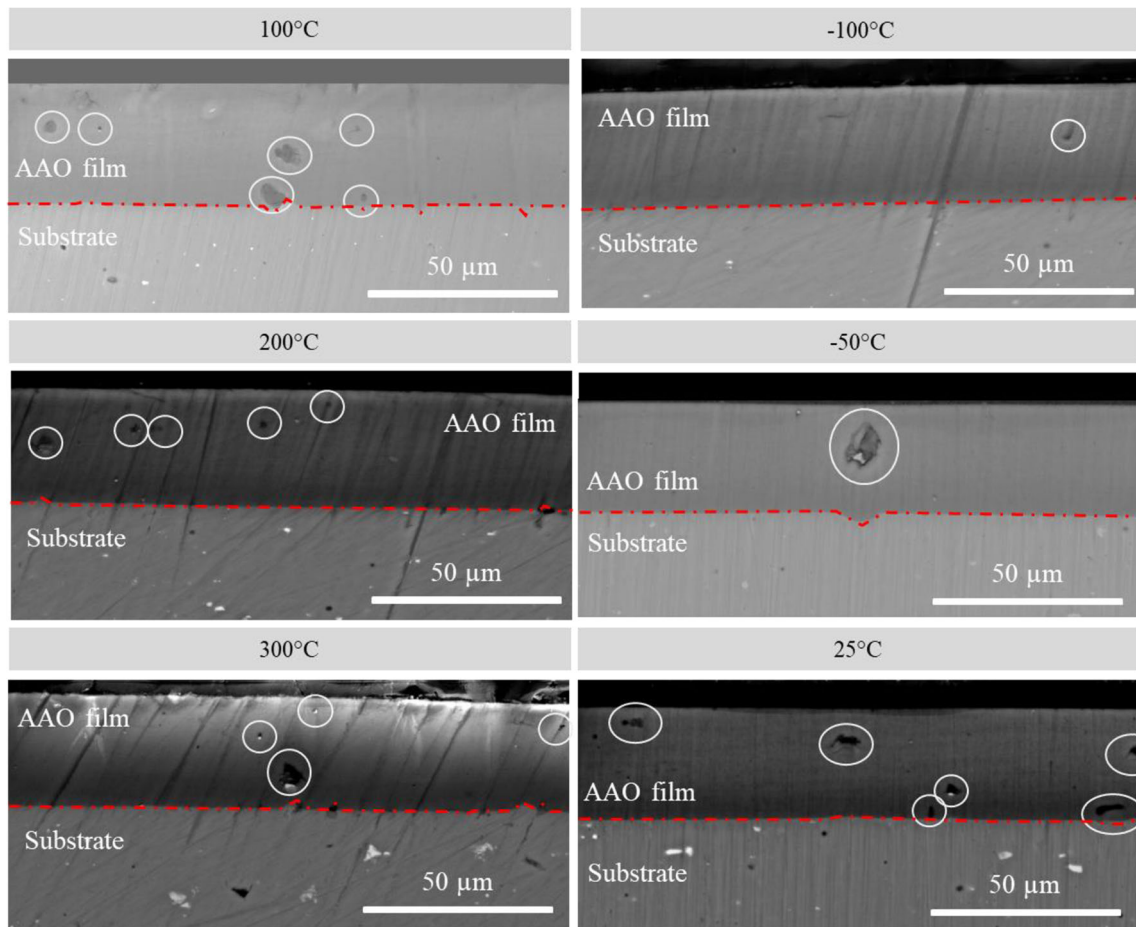
Fig. 24 SEM images of the cross-section of the AAO specimens at varying testing temperature
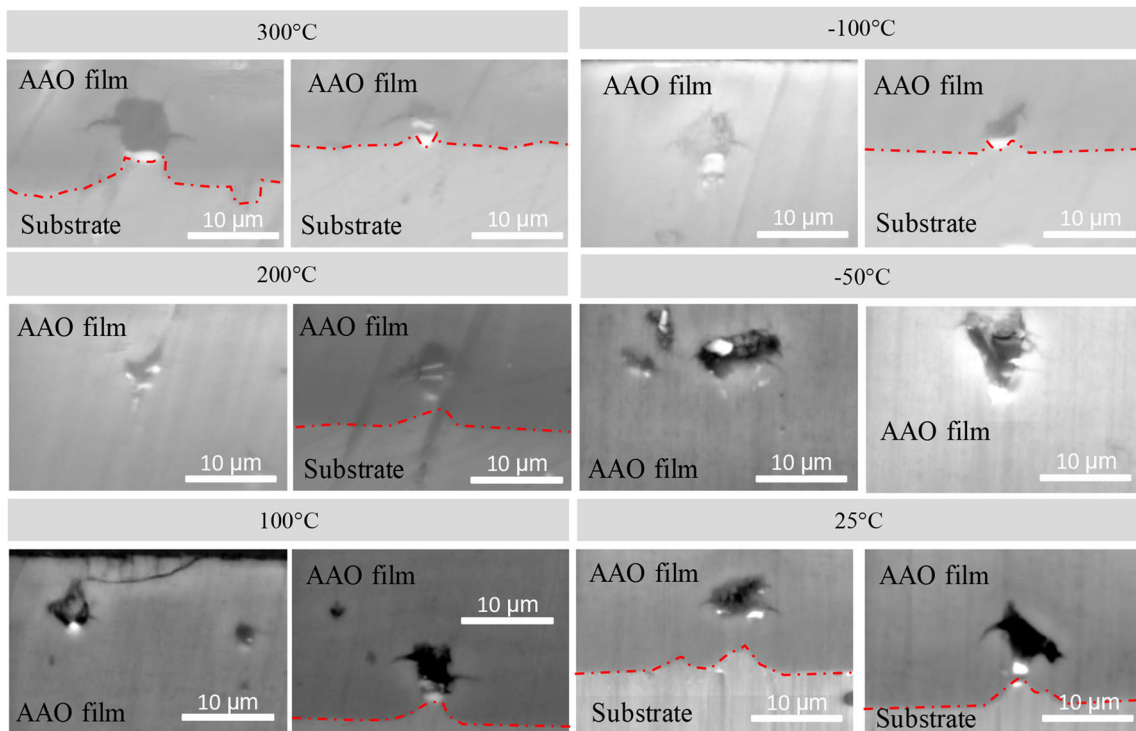

Fig. 25 Magnified SEM images of the defects present on the cross-section of the AAO specimens at varying testing temperature

Table 4 EDS analysis of the IMPs trapped in the AAO film of different specimens visible in Fig. 29

No.	Al	O	Fe	Cu	Si	Mg	S	C	Zn
1	57.1	24.0	8.2	3.0	-	2.8	3.3	-	1.6
2	13.7	24.4	-	-	-	-	1.6	60.3	-
3	44.5	45.5	-	-	2.3	1.7	6.0	-	-
4	78.2	8.4	2.0	2.0	1.3	2.7	1.0	-	4.4

of flaws as visible in both Fig. 26 a and b. Along with nobility, also the specific electrical resistivity of the particles is of primary importance: among the particles reported in Table 4, silicon possesses the lowest one. This has influenced the film formation as follows: when the anodization process starts, the Mg-Si IMPs have different dissolution rates since magnesium is characterized by a lower ionization energy compared to silicon [46]. The magnesium atoms are incorporated within the AAO film or are eventually expelled in the electrolyte bath. Mg-Si particles gradually reduce up to form a single silicon particle, which remains in situ as shown in Fig. 26b. This leads to an intense corrosion current density that favours the dissolution of the aluminium atoms and contributes to the formation of the concave film.

3.7 Corrosion resistance after anodization

The polarization curves of the AA7075-T6 specimens after anodization are shown in Fig. 27, whereas Table 5 reports the electrochemical corrosion data. Above E_{corr}, the current density increases slowly and oscillates until reaching the pitting potential after which it rapidly increases.

As expected, the corrosion resistance after anodization is improved compared to the value after just mechanical deformation (Fig. 19). The reduction percentage relative to the corrosion current density before and after AAO settles to approximately 99%, regardless of the testing temperature.
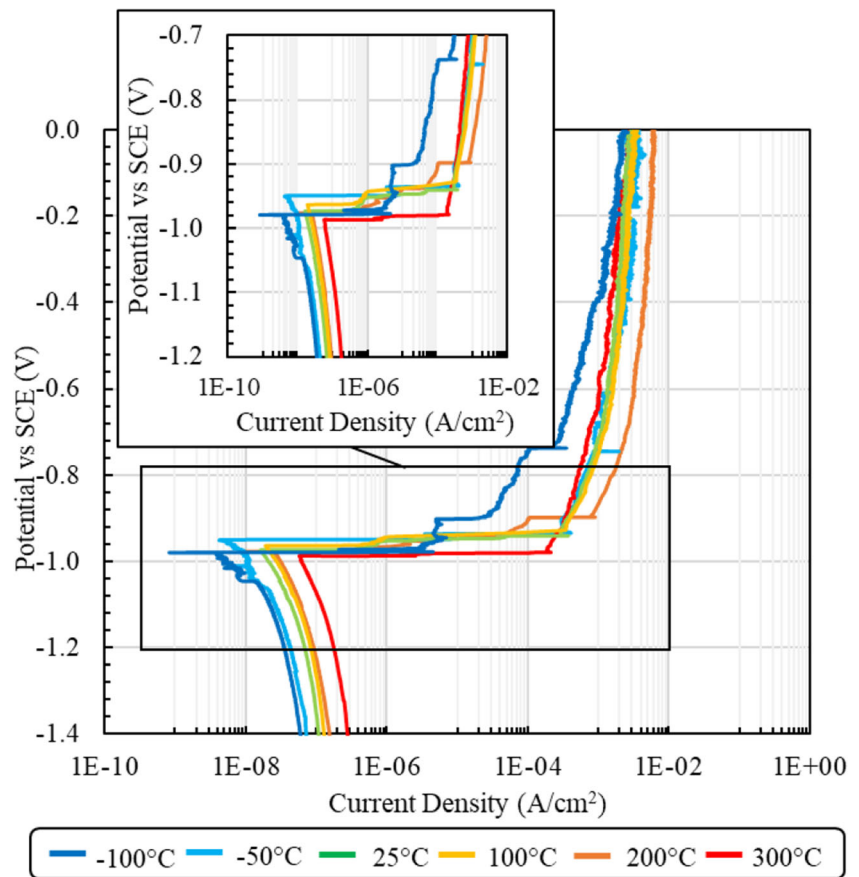
Table 5 shows that the mechanical testing temperature has a great influence on the corrosion resistance of the AAO specimens, especially in terms of $Icorr$. Actually, the specimen deformed at −100°C presented the lowest $Icorr$, providing a reduction of 95%, 82%, 80%, 73% and 20% compared to the specimens deformed at 300°C, 200°C, 100°C, 25°C and −50°C, respectively.

Specifically, an exponential relationship was found to correlate $Icorr$ and the mechanical testing temperature ($R^2=0.93$) and is shown in Fig. 28.
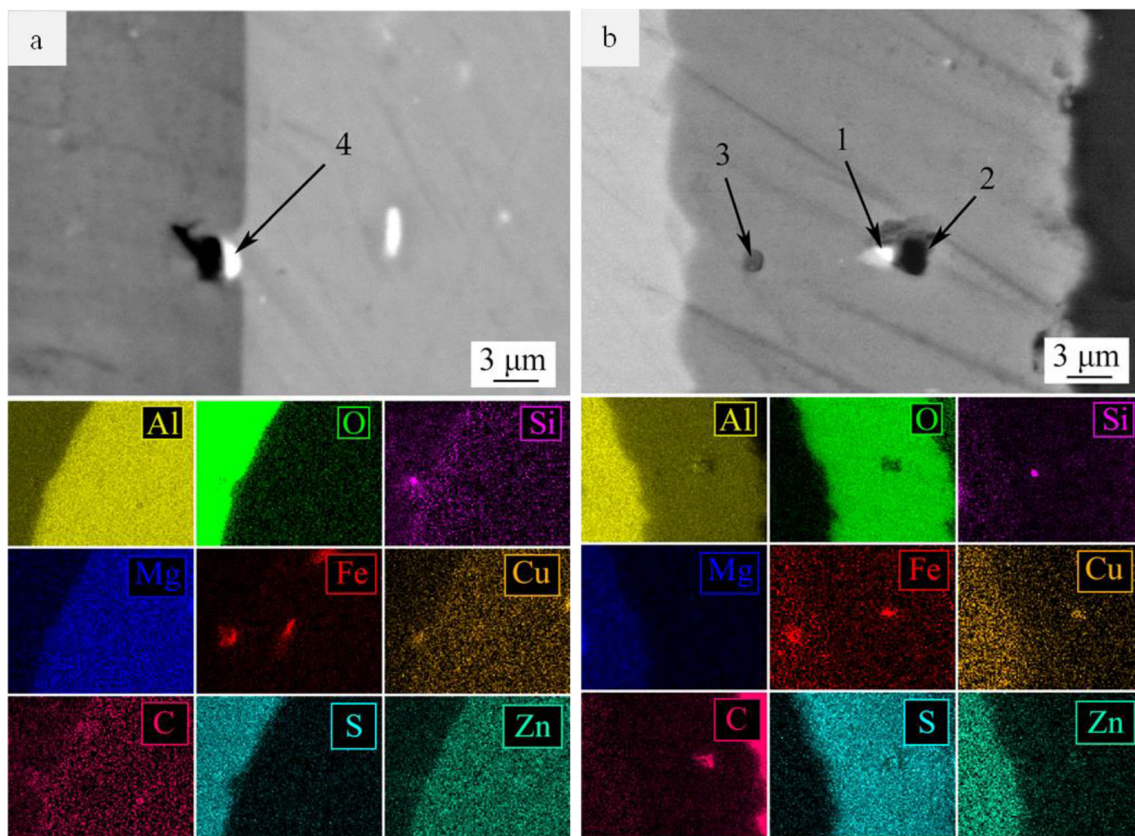
Fig. 26 EDS maps associated with the SEM images of the specimens UTS-deformed at **a** −100°C and **b** 300°C

Fig. 27 Potentiodynamic polarization curves of the specimens after anodization at varying testing temperature

## 3.8 Anodization improvement at varying testing temperature

The corrosion resistance after anodization results strictly dependent upon the mechanical testing temperature as demonstrated in Fig. 27 and Table 5. As a matter of fact, different surface roughness, AAO layer thickness and density of defects within the AAO layer were noticed after mechanical deformation. In the following, the contribution of each of these factors in affecting the corrosion resistance is discussed in detail.

It is generally recognized that high values of the average surface roughness reduce the corrosion resistance since the higher the roughness, the higher the contact area between the surface and the corrosive environment. Nevertheless, it may not be true when the differences between values are restrained [47]. In the present study, the specimen deformed at −100°C was characterized by the roughest surface but the highest corrosion resistance, suggesting no correlation between them. On the contrary, the surface roughness of the

Table 5 Electrochemical data obtained from potentiodynamic polarization curves after anodization at varying testing temperature

Testing temperature (°C)	I_{corr} (µA/cm^2)	E_{corr} (V)
−100	0.008 ± 0.001	−0.98 ± 0.05
−50	0.01± 0.02	−0.95 0.05
25	0.03± 0.02	−0.98 0.05
100	0.04± 0.01	−0.96 0.06
200	0.045± 0.02	−0.98 0.05
300	0.15± 0.07	−0.98 0.06
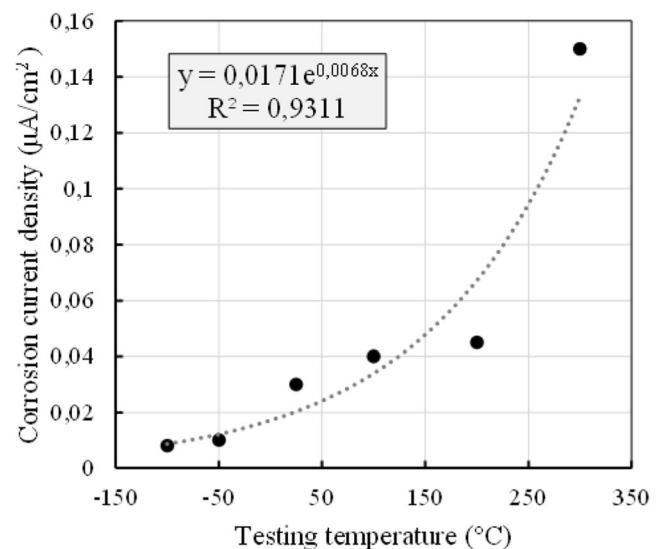
Fig. 28 Correlation between *Icorr* and mechanical testing temperature

other specimens settled to comparable values, but their electrochemical behaviour was completely different.

In general, the thicker the oxide coating layer, the higher the corrosion resistance due to its higher stability [48]. Nevertheless, in the present study, a correlation was not found between the thickness of AAO layer and the corrosion performances. The reason is attributed to the fact that the differences in the AAO thickness were limited to a maximum of 9% (see Fig. 23).

The trigger of pitting corrosion is often connected to the presence of surface defects, like flaws in the oxide or alloying elements segregation, as well as the presence of aggressive chloride anions in the environment. Actually, during polarization tests, chlorine ions are able to penetrate across voids and gas pockets as preferential path. Therefore, defects on the AAO layer represent an easy path for corrosion. In the present study, the specimen deformed at −100°C was more corrosion resistant than the others, which is attributed to the presence of less and finer IMPs after deformation, which minimizes the possible attacks from the corrosive environment. On the contrary, the specimen deformed at 300°C showed coalescence of particles and scarce corrosion resistance.

In [13], polarization curves were recorded for AA6066 after cryogenic forging (CFT6) and compared to the bare alloy (T6). The T6 specimen reported almost an increase of an order of magnitude in the corrosion current density compared to the one of the CFT6. The reason was attributed to the higher number of coarse second phase and IMPs that characterized the T6 alloy, which favoured the entrapment of air pockets

acting as corrosion paths to accelerate the chloride attacks. The same conclusions were achieved in [14] in which cryogenic rolling of 7075-T73 alloy was compared to room temperature rolling in terms of microstructure, mechanical properties and corrosion resistance. Cryogenic rolling was found to sensibly improve the corrosion resistance even compared to the as-delivered condition. Particles containing silicon were claimed to be the dominant factor to control corrosion, since they were only partially sealed, and cryo-rolling contributed to sensibly decrease the number of those particles.

On the basis of what aforementioned, it can be said that the size and density of IMPs play the predominant role in conditioning the corrosion resistance of the AA7075-T6 after deformation and anodization.

3.9 Overall evaluation of the effect of the mechanical testing temperature

Figure 29 displays the effect of the testing temperature on the AA7075-T6 mechanical properties and corrosion resistance arranged on the experimental findings of this study. In this chart, each parameter is equally weighted and is located considering that the values on the outer layers guarantee improved mechanical and corrosion characteristics. It is worth noting that the other outcomes of the experimental characterization were not considered since they indirectly affect the mechanical behaviour and corrosion resistance of the alloy. The corrosion current density pre- and post-AAO was rearranged as

Fig. 29 Radar plots for the AA7075-T6 alloy characteristics at varying testing temperature
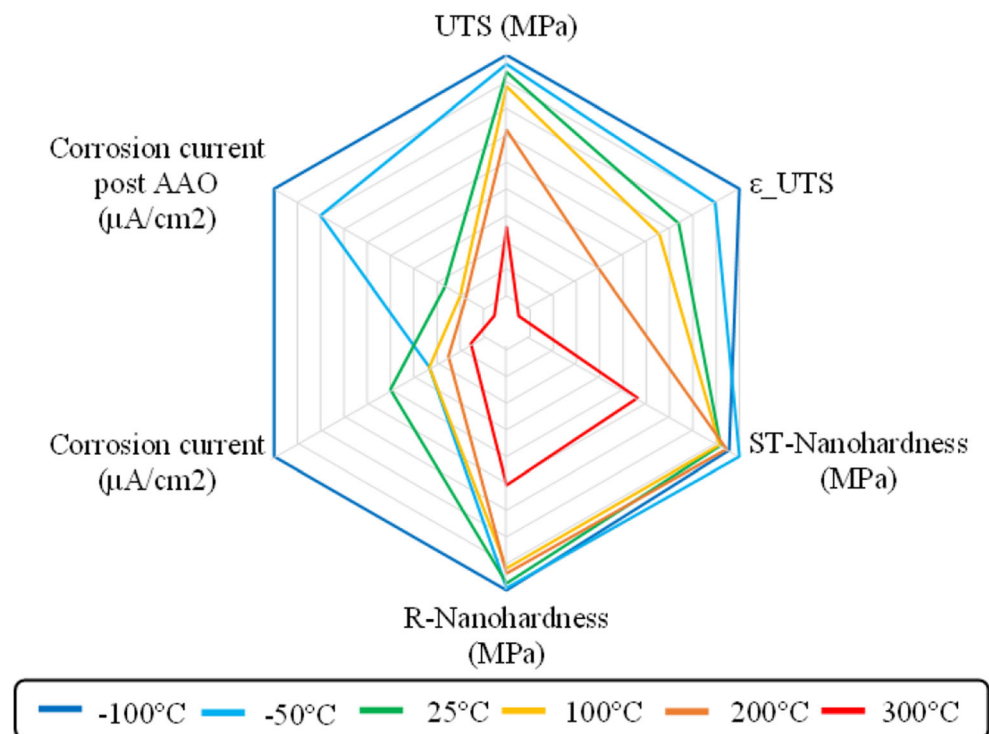
its relative so to its higher value corresponds an enhancement of the corrosion resistance.

On the basis of these considerations, −100°C is the forming temperature that allows achieving the best performances, since its curves maximize all the considered variables. The worst performances pertain to the case of 300°C testing temperature, while the other temperatures lie in between.

In the case of aluminium and its alloys, warm temperature settles in between the recrystallization temperature [9] and 0.3 times of the melting temperature [49]. To this regime both 200°C and 300°C belong. As a consequence of the sensible decrease in the AA7075-T6 mechanical properties, especially at 300°C (see Fig. 18), a post-forming heat treatment is surely necessary, with a consequent increase of the manufacturing chain steps and, therefore, time and costs. The other testing temperatures belong to the cold regime, which can be further subdivided in sub-zero and up-zero temperatures. In the case of 25°C and 100°C, the uniform elongation is only slightly increased compared to the one in the warm regime, therefore not providing a useful improvement with the respect of the alloy formability. Finally, the sub-zero temperature regime refers to −50°C and −100°C: even if contained differences are seen with the respect of the mechanical properties, a great difference is seen in the case of the corrosion resistance. To this reason, −100°C is the temperature suggested to carry out manufacturing process in order to obtain, at the same time, an improvement in both mechanical properties and corrosion resistance.

4 Conclusions

In the present work, the effect of sheet stamping temperatures on the mechanical, corrosion and anodization behaviour of the AA7075-T6 aluminium alloy was investigated. Uniaxial tensile tests were performed at −100°, −50°C, 0°C, 25°C, 100°C, 200°C and 300 °C at varying rolling directions. The characterization of the deformed material was assessed by means of microstructural investigations and nano-hardness measurements. Afterwards, the UTS-deformed specimens were subjected to AAO process, typically applied to aerospace components, and then their corrosion performances were evaluated.

The following conclusions can be drawn:

- An average increase of the UTS of about 6.6% was found at the lowest testing temperature, with a maximum of 6.9% along the 45° direction, if compared with the room temperatures tests.
- An average increase of ε^{neck} of 28.6% was registered at −100°C if compared with the room temperature case. Specifically, a maximum of 35.2% was obtained along the rolling direction.

- An increase of the strain at necking ε^{neck} as the applied temperature decreased was found regardless of the rolling direction.
- No alteration of the grain size was highlighted for deformations carried out under 200°C, with respect to the as-delivered state.
- The texture was not significantly affected by the deformation temperatures since it did not vary from the one of the as-received sheets.
- The −100°C UTS-deformed specimen showed a higher fraction of LAGBs with respect to the 200°C, witnessing a higher deformed state within the material. Similarly, larger fraction of disorientated angles was found in the specimen deformed at low temperature due to the higher dislocation density.
- The highest temperature deformation contributed to increase the number of large IMPs as well as intermetallic particles, whereas the lowest one induced their fragmentation.
- Harder surfaces were obtained at sub-zero temperatures, with an increase of 11% compared to the starting material along the ST plane. On the contrary, softer surfaces are obtained when deforming within the warm regime with a decrease of 35% with the respect of the starting material.
- The highest temperature deformation, namely 200°C and 300°C, induced a corrosion resistance reduction, by increasing the *Icorr*. For example, an 85% decrease in *Icorr* was registered from −100 to 300°C deformation temperature.
- The surface roughness of the AAO layer as well as its thickness were not correlated with the deformation testing temperature. On the contrary, the density of defects appeared to be matrix-dependent. In fact, these defects arise from the different nobility of IMP particles whose distribution was determined by the deformation temperature.
- The corrosion resistance improved approximately 99% after anodization, regardless of the deformation temperature. Nevertheless, an exponential relationship was found to correlate *Icorr* to the mechanical testing temperature, being the specimen deformed at −100°C noticeably less prone to be corroded compared to the one deformed at 300°C.
- Overall, −100°C appears as the deformation temperature able to increase the formability, nano-hardness and corrosion resistance before and after anodization of the AA7075 alloy.

Enrico Simonetto: Methodology, investigation, formal analysis, data curation, writing-original draft

Luca Pezzato: Data curation and writing-original draft

Alberto Fabrizi: Data curation and writing-original draft

Andrea Ghiotti: Conceptualization, writing-reviewing and editing, supervision, and project administration

Stefania Bruschi: Writing-reviewing and editing, supervision, and project administration

Declarations

Ethics approval Not applicable.

Consent to participate The authors declare their consent to participate.

Consent for publication The authors declare their consent for publication.

Competing interests The authors declare no competing interests.

References

1. Birol Y, Gokcil E, Guvenc MA, Akdi S (2016) Processing of high strength EN AW 6082 forgings without a solution heat treatment. Mater Sci Eng A 674:25–32. https://doi.org/10.1016/j.msea.2016.07.062

2. J. Imbert, M. Worswick, S. Winkler, S. Golovashchenko, V. Dmitriev, Analysis of the increased formability of aluminum alloy sheet formed using electromagnetic forming, SAE Tech. Pap. (2005) 2005-01-0082. https://doi.org/10.4271/2005-01-0082.

3. Starke EA, Staley JT (2010) Application of modern aluminium alloys to aircraft. Woodhead Publishing Limited. https://doi.org/10.1533/9780857090256.3.747

4. Reviewed P, Berkeley L, Cancer B (1987) Mechanical behavior of aluminum-lithium alloys at cryogenic temperatures. Metall Trans A 18:1695–1701

5. Keeler SP (1966) Determination of forming limits in automotive stampings. SAE Tech. Pap. 74:1–9. https://doi.org/10.4271/650535

6. Abachi P, Naseri PSZ, Purazrang K, Coyle TW (2016) Fracture behavior evaluation of high-strength 7050 and 7075 aluminum alloys using V-notched specimen. Fract. Mech. - Prop. Patterns Behav 147. https://doi.org/10.5772/64463

7. Pedersen KO, Børvik T, Hopperstad OS (2011) Fracture mechanisms of aluminium alloy AA7075-T651 under various loading conditions. Mater. Des. 32:97–107. https://doi.org/10.1016/j.matdes.2010.06.029

8. Simonetto E, Bertolini R, Ghiotti A, Bruschi S (2020) Mechanical and microstructural behaviour of AA7075 aluminium alloy for sub-zero temperature sheet stamping process. Int. J. Mech. Sci. 187:105919. https://doi.org/10.1016/j.ijmecsci.2020.105919

9. Maeno T, Mori K, Yachi R (2017) Hot stamping of high-strength aluminium alloy aircraft parts using quick heating. CIRP Ann. - Manuf. Technol. 66:269–272. https://doi.org/10.1016/j.cirp.2017.04.117

10. Wang A, Zhong K, El Fakir O, Liu J, Sun C, Wang LL, Lin J, Dean TA (2017) Springback analysis of AA5754 after hot stamping: experiments and FE modelling. Int. J. Adv. Manuf. Technol. 89:1339–1352. https://doi.org/10.1007/s00170-016-9166-3

11. Fan X, He Z, Zheng K, Yuan S (2015) Strengthening behavior of Al-Cu-Mg alloy sheet in hot forming-quenching integrated process with cold-hot dies. Mater. Des. 83:557–565. https://doi.org/10.1016/j.matdes.2015.06.058

12. Shih TS, Yong HS, Hsu WN (2016) Effects of cryogenic forging and anodization on the mechanical properties and corrosion resistance of AA6066-T6 aluminum alloys. Metals 6:51. https://doi.org/10.3390/met6030051

13. Sen Huang Y, Shih TS, Chou JH (2013) Electrochemical behavior of anodized AA7075-T73 alloys as affected by the matrix structure. Appl. Surf. Sci. 283:249–257. https://doi.org/10.1016/j.apsusc.2013.06.094

14. Kumar N, Rao PN, Jayaganthan R, Brokmeier HG (2015) Effect of cryorolling and annealing on recovery, recrystallisation, grain growth and their influence on mechanical and corrosion behaviour of 6082 Al alloy. Materials Chemistry and Physics 165:177–187

15. Zoqui EJ, Torres LV (2010) Evaluation of the thixoformability of AA7004 and AA7075 alloys. Mater Res 13(3):305–318. https://doi.org/10.1590/s1516-14392010000300006

16. Singh SS, Guo E, Xie H, Chawla N (2015) Mechanical properties of intermetallic inclusions in Al 7075 alloys by micropillar compression. Intermetallics. 62:69–75. https://doi.org/10.1016/j.intermet.2015.03.008

17. Ahmed MMZ, Ataya S, El-Sayed Seleman MM, Ammar HR, Ahmed E (2017) Friction stir welding of similar and dissimilar AA7075 and AA5083. J. Mater. Process. Technol. 242:77–91. https://doi.org/10.1016/j.jmatprotec.2016.11.024

18. Aegerter J, Kühn HJ, Frenz H, Weißmüller C (2011) EN ISO 6892-1: 2009 tensile testing: initial experience from the practical implementation of the new standard. Materials Testing 53(10):595–603

19. Bariani PF, Bruschi S, Ghiotti A, Michieletto F (2013) Hot stamping of AA5083 aluminium alloy sheets. CIRP Ann. - Manuf. Technol. 62:251–254. https://doi.org/10.1016/j.cirp.2013.03.050

20. Wang JS, Hsieh CC, Lin CM, Chen EC, Kuo CW, Wu W (2014) The effect of residual stress relaxation by the vibratory stress relief technique on the textures of grains in AA 6061 aluminum alloy. Mater. Sci. Eng. A. 605:98–107. https://doi.org/10.1016/j.msea.2014.03.037

21. Chen P, Mao SC, Liu Y, Wang F, Zhang YF, Zhang Z, Han XD (2013) In-situ EBSD study of the active slip systems and lattice rotation behavior of surface grains in aluminum alloy during tensile deformation. Mater. Sci. Eng. A. 580:114–124. https://doi.org/10.1016/j.msea.2013.05.046

22. ASTM G5 - 14e1: Standard reference test method for making potentiodynamic anodic polarization measurements.

23. Lu J, Song Y, Hua L, Zheng K, Dai D (2018) Thermal deformation behavior and processing maps of 7075 aluminum alloy sheet based on isothermal uniaxial tensile tests. J. Alloys Compd. 767:856–869. https://doi.org/10.1016/j.jallcom.2018.07.173

24. Kumar M, Sotirov N, Grabner F, Schneider R, Mozdzen G (2017) Cryogenic forming behaviour of AW-6016-T4 sheet. Trans.

Nonferrous Met. Soc. China 27:1257–1263. https://doi.org/10.1016/S1003-6326(17)60146-8

25. Rometsch PA, Zhang Y, Knight S (2014) Heat treatment of 7xxx series aluminium alloys - some recent developments. Trans. Nonferrous Met. Soc. China 24:2003–2017. https://doi.org/10.1016/S1003-6326(14)63306-9

26. Panigrahi SK, Jayaganthan R (2011) Effect of ageing on microstructure and mechanical properties of bulk, cryorolled, and room temperature rolled Al 7075 alloy. J. Alloys Compd. 509:9609–9616. https://doi.org/10.1016/j.jallcom.2011.07.028

27. Ghosh A, Ghosh M, Shankar G (2018) On the role of precipitates in controlling microstructure and mechanical properties of Ag and Sn added 7075 alloys during artificial ageing. Mater. Sci. Eng. A. 738:399–411. https://doi.org/10.1016/j.msea.2018.09.109

28. Ma K, Wen H, Hu T, Topping TD, Isheim D, Seidman DN, Lavernia EJ, Schoenung JM (2014) Mechanical behavior and strengthening mechanisms in ultrafine grain precipitation-strengthened aluminum alloy. Acta Mater. 62:141–155. https://doi.org/10.1016/j.actamat.2013.09.042

29. Xu X, Zhao Y, Wang X, Zhang Y, Ning Y (2015) The rapid age strengthening induced by Ag additions in 7075 aluminum alloy. Mater. Sci. Eng. A. 648:367–370. https://doi.org/10.1016/j.msea.2015.09.044

30. Muzyk M, Pakiela Z, Kurzydlowski KJ (2011) Ab initio calculations of the generalized stacking fault energy in aluminium alloys. Scr. Mater. 64:916–918. https://doi.org/10.1016/j.scriptamat.2011.01.034

31. Han D, He JX, Guan XJ, Zhang YJ, Li XW (2019) Impact of short-range clustering on the multistage work-hardening behavior in Cu–Ni alloys. Metals 9:11–15. https://doi.org/10.3390/met9020151

32. Szklarska-Smialowska Z (1999) Pitting corrosion of aluminum. Corros. Sci. 41:1743–1767. https://doi.org/10.1016/S0010-938X(99)00012-8

33. Holroyd NJH, Hardie D (1983) Factors controlling crack velocity in 7000 series aluminium alloys during fatigue in an aggressive environment. Corros. Sci 23. https://doi.org/10.1016/0010-938X(83)90117-8

34. Chen GS, Gao M, Wei RP (1996) Microconstituent-induced pitting corrosion in aluminum alloy 2024-T3. Corros. 52:8–15. https://doi.org/10.5006/1.3292099

35. Birbilis N, Cavanaugh MK, Buchheit RG (2006) Electrochemical behavior and localized corrosion associated with Al7Cu2Fe particles in aluminum alloy 7075-T651. Corros. Sci. 48:4202–4215. https://doi.org/10.1016/j.corsci.2006.02.007

36. Li JF, Zheng ZQ, Li SC, Chen WJ, Ren WD, Zhao XS (2007) Simulation study on function mechanism of some precipitates in localized corrosion of Al alloys. Corros. Sci. 49:2436–2449. https://doi.org/10.1016/j.corsci.2006.12.002

37. Zhu Y, Frankel GS, Zhu Y, G. S. (2019) Frankel, Effect of major intermetallic particles on localized corrosion of AA2060-T8. Corros. 75:29–41. https://doi.org/10.5006/2867

38. Birbilis N, Buchheit RG (2005) Electrochemical characteristics of intermetallic phases in aluminum alloys. J. Electrochem. Soc. 152:B140. https://doi.org/10.1149/1.1869984

39. Son IJ, Nakano H, Oue S, Kobayashi S, Fukushima H, Horita Z (2008) Pitting corrosion resistance of anodized aluminum-copper alloy processed by severe plastic deformation. Mater. Trans. 49:2648–2655. https://doi.org/10.2320/matertrans.MRA2008216

40. Chemin A, Marques D, Bisanha L, Motheo AJ, Filho WWB, Ruchert COF (2014) Influence of Al7Cu2Fe intermetallic particles on the localized corrosion of high strength aluminum alloys. Mater. Des. 53:118–123. https://doi.org/10.1016/j.matdes.2013.07.003

41. Rangaraju N, Raghuram T, Krishna BV, Rao KP, Venugopal P (2005) Effect of cryo-rolling and annealing on microstructure and properties of commercially pure aluminium. Mater. Sci. Eng. A. 398:246–251. https://doi.org/10.1016/j.msea.2005.03.026

42. Talianker M, Cina B (1989) Retrogression and reaging and the role of dislocations in the stress corrosion of 7000-type aluminum alloys. Metall. Trans. A. 20:2087–2092. https://doi.org/10.1007/BF02650294

43. Schütze, M, Dietrich Wieser, and Roman Bender, eds (2010) Corrosion resistance of aluminium and aluminium alloys. John Wiley & Sons

44. Zhang F, Örnek C, Nilsson JO, Pan J (2020) Anodisation of aluminium alloy AA7075 – influence of intermetallic particles on anodic oxide growth. Corros. Sci. 164:108319. https://doi.org/10.1016/j.corsci.2019.108319

45. Soisrihaa P, Akaratatreepongb P, Threrujirapapongc T, Leelachaod S, Taweesupe K, Visuttipitukulf P (2018) Influence of anodizing current on structure and color intensity of anodized aluminium alloys, 2018 2nd Int. Conf. Eng. Innov. ICEI 2018:106–110. https://doi.org/10.1109/ICEI18.2018.8448843

46. Fratila-Apachitei LE, Tichelaar FD, Thompson GE, Terryn H, Skeldon P, Duszczyk J, Katgerman L (2004) A transmission electron microscopy study of hard anodic oxide layers on AlSi(Cu) alloys. Electrochim. Acta. 49:3169–3177. https://doi.org/10.1016/j.electacta.2004.02.030

47. Bertolini R, Bedekar V, Ghiotti A, Savio E, Shivpuri R, Bruschi S (2020) Surface integrity and corrosion performances of hardened bearing steel after hard turning. Int. J. Adv. Manuf. Technol. 108:1983–1995. https://doi.org/10.1007/s00170-020-05352-4

48. Cirik E, Genel K (2008) Effect of anodic oxidation on fatigue performance of 7075-T6 alloy. Surf. Coatings Technol. 202:5190–5201. https://doi.org/10.1016/j.surfcoat.2008.06.049

49. Lin J, Liu Y, Dean TA (2005) A review on damage mechanisms, models and calibration methods under various deformation conditions. Int. J. Damage Mech. 14:299–319. https://doi.org/10.1177/1056789505050357